Ryanodine Receptor Allosteric Coupling and the Dynamics of Calcium Sparks

Jeffrey R. Groff* and Gregory D. Smith*†
*Department of Applied Science, College of William and Mary, Williamsburg, Virginia; and †Mathematical Biosciences Institute, Ohio State University, Columbus, Ohio

ABSTRACT Puffs and sparks are localized intracellular Ca^{2+} elevations that arise from the cooperative activity of Ca^{2+}-regulated inositol 1,4,5-trisphosphate receptors and ryanodine receptors clustered at Ca^{2+} release sites on the surface of the endoplasmic reticulum or the sarcoplasmic reticulum. While the synchronous gating of Ca^{2+}-regulated Ca^{2+} channels can be mediated entirely though the buffered diffusion of intracellular Ca^{2+}, interprotein allosteric interactions also contribute to the dynamics of ryanodine receptor (RyR) gating and Ca^{2+} sparks. In this article, Markov chain models of Ca^{2+} release sites are used to investigate how the statistics of Ca^{2+} spark generation and termination are related to the coupling of RyRs via local $[Ca^{2+}]$ changes and allosteric interactions. Allosteric interactions are included in a manner that promotes the synchronous gating of channels by stabilizing neighboring closed-closed and/or open-open channel pairs. When the strength of Ca^{2+}-mediated channel coupling is systematically varied (e.g., by changing the Ca^{2+} buffer concentration), simulations that include synchronizing allosteric interactions often exhibit more robust Ca^{2+} sparks; however, for some Ca^{2+} coupling strengths the sparks are less robust. We find no evidence that the distribution of spark durations can be used to distinguish between allosteric interactions that stabilize closed channel pairs, open channel pairs, or both in a balanced fashion. On the other hand, the changes in spark duration, interspark interval, and frequency observed when allosteric interactions that stabilize closed channel pairs are gradually removed from simulations are qualitatively different than the changes observed when open or both closed and open channel pairs are stabilized. Thus, our simulations clarify how changes in spark statistics due to pharmacological washout of the accessory proteins mediating allosteric coupling may indicate the type of synchronizing allosteric interactions exhibited by physically coupled RyRs. We also investigate the validity of a mean-field reduction applicable to the dynamics of a ryanodine receptor cluster coupled via local $[Ca^{2+}]$ and allosteric interactions. In addition to facilitating parameter studies of the effect of allosteric coupling on spark statistics, the derivation of the mean-field model establishes the correct functional form for cooperativity factors representing the coupled gating of RyRs. This mean-field formulation is well suited for use in computationally efficient whole cell simulations of excitation-contraction coupling.

INTRODUCTION

Localized intracellular Ca^{2+} elevations, known as puffs and sparks, are cellular signals of great interest that arise from the cooperative activity of clusters of Ca^{2+}-regulated inositol 1,4,5-trisphosphate receptors and ryanodine receptors (RyRs). Not only are puffs, sparks, and other localized Ca^{2+} elevations highly specific regulators of cellular function, they also contribute to global Ca^{2+} release events in eukaryotic cells (1–6). For example, the process of excitation-contraction (EC) coupling in cardiac myocytes is initiated when electrical depolarization of the sarcolemma allows a small amount of Ca^{2+} to enter the cell via voltage-gated L-type Ca^{2+} channels (dihydropyridine receptors). This trigger Ca^{2+} activates a much larger release of Ca^{2+} from the sarcoplasmic reticulum (SR) via Ca^{2+}-activated RyRs clustered at a Ca^{2+} release site, a process known as Ca^{2+}-induced Ca^{2+}-release, resulting in a Ca^{2+} spark. Although the increase in $[Ca^{2+}]$ due to individual sparks is localized to Ca^{2+} release sites, the cell-wide summation of many sparks provides the increase in the cytosolic $[Ca^{2+}]$ that initiates the mechanical contraction of the myocyte.

Experimental evidence suggests that the dynamics of RyR gating, Ca^{2+} sparks, and EC coupling are affected by interprotein allosteric interactions between neighboring RyRs at Ca^{2+} release sites. Each RyR channel is an oligomer composed of four identical 565 kDa RyR proteins surrounding a central pore, and groups of 10–100 RyR homotetramers form regular two-dimensional checkerboard-like lattices on the surface of the SR membrane (4,7–12) (see Fig. 1 *A*). When channels are reconstituted to mimic this in situ crystalline lattice, RyRs maintain physical contact with neighboring channels (9). Moreover, Marx and co-workers observed that physically coupled RyRs incorporated into planar lipid bilayers exhibit coupled gating even when Ca^{2+} is not the charge carrier (13,14). While such Ca^{2+}-independent coupling has not been uniformly observed in other labs (15,16), functional coupling may require the association of FK-binding proteins (FKBPs) that conjugate with the RyR homotetramer in approximately stoichiometric proportions (16–18).

The biophysical theory connecting single-channel kinetics of inositol 1,4,5-trisphosphate receptors and RyRs to the collective phenomena of Ca^{2+} puffs and sparks and global phenomena such as EC coupling is not as well developed as our understanding of the association of Ca^{2+} with endo-

Submitted August 19, 2007, and accepted for publication March 10, 2008.

Address reprint requests to Greg D. Smith, Tel.: 757-221-1989; E-mail: greg@as.wm.edu.

Editor: Ian Parker.

0006-3495/08/07/135/20 $2.00

doi: 10.1529/biophysj.107.119982

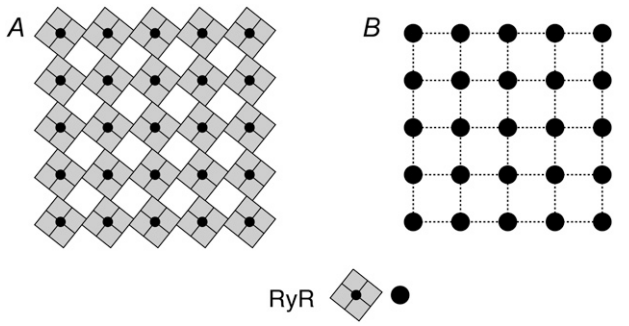

FIGURE 1 (*A*) Schematic representation of a Ca^{2+} release site following Yin et al. (9). Each ryanodine receptor Ca^{2+} release channel (RyR) is composed of four identical subunits (*shaded squares*) surrounding a central pore (*solid circle*). Subunits physically contact neighboring subunits and homotetrameric channels form a right-handed checkerboard-like lattice. (*B*) In the Ca^{2+} release site model, two-state Ca^{2+}-activated RyRs (*solid circles*) are globally coupled via the buffered diffusion of intracellular Ca^{2+} (not shown) and locally coupled to 2–4 nearest neighbors via allosteric interactions (*dotted lines*). Consistent with experimentally measured RyR lattice dimensions, the pore-to-pore interchannel distance is 30 nm.

genous and exogenous buffers (e.g., Ca^{2+}-binding proteins, chelators, and indicators) (19–27). However, several theoretical studies have demonstrated that dynamics reminiscent of Ca^{2+} puffs and sparks may arise due to the cooperative activity of a cluster of Ca^{2+}-regulated Ca^{2+}-release channels modeled as a continuous-time discrete-state Markov chain (28–38). In such simulations, individual Ca^{2+}-release channels are coupled via a time-dependent or time-independent representation of the local $[Ca^{2+}]$, the so-called Ca^{2+} microdomain, and exhibit stochastic Ca^{2+} excitability where channels open and close in a concerted fashion. The phenomena of Ca^{2+} activation and inactivation, the dynamics of the buffered diffusion of intracellular Ca^{2+}, and the release site density and geometry, all significantly contribute to the statistics of simulated puffs and sparks (31,38,39).

Several theoretical studies to date have investigated the effects of interprotein allosteric coupling on the dynamics of Ca^{2+} sparks. Stern et al. demonstrated that models of single channel gating derived from planar lipid bilayer experiments fail to produce stable EC coupling in release site models (36). However, when release site models include nearest-neighbor allosteric interactions in addition to Ca^{2+} coupling, Ca^{2+} sparks can be recovered (36). Allosteric couplings in Stern et al. (36) are defined as free energies of interactions between neighboring channels and have the effect of modifying the affinity of release site transitions.

Using a formulation for allosteric coupling that is minimal compared to Stern's, Sobie et al. (40) studied the effects of allosteric interactions on spark statistics such as duration and frequency. This sticky-cluster model of Ca^{2+}-induced Ca^{2+} release includes so-called coupling factors that scale the transition rates of the single channel model allowing the gating of each channel to be influenced by the number of open and closed RyRs at the release site. Although these coupling factors are post hoc additions to the single-channel RyR model, and there is no account of release site geometry or nearest-neighbor interactions, the sticky-cluster model demonstrated that allosteric coupling may contribute to spark termination.

To clarify how the microscopic parameters of allosteric interactions and Ca^{2+} coupling simultaneously contribute to the generation and termination of spontaneous Ca^{2+} sparks, we construct and analyze release site models composed of 16–49 two-state Ca^{2+}-activated RyRs organized on a Cartesian lattice and instantaneously coupled using linearized equations for the buffered diffusion of microdomain Ca^{2+} (25). Using the methodology introduced by Stern et al. (36), RyRs also experience nearest-neighbor allosteric interactions that promote synchronous gating of channels (see Fig. 1 *B*). Importantly, these synchronizing allosteric interactions may be incorporated to stabilize closed channel pairs, open channel pairs, or both in a balanced fashion. We probe how these different types of synchronizing allosteric interactions affect the presence or absence of Ca^{2+} excitability and the statistics of spontaneous Ca^{2+} sparks. In addition, we derive and validate a mean-field modeling approach that is applicable to the dynamics of RyR clusters coupled via microdomain Ca^{2+} and nearest-neighbor allosteric interactions. Similar to the sticky-cluster model presented by Sobie et al. (40), the mean-field approach aggregates states based on the number of open RyRs at a Ca^{2+} release site; however, the coupling factors representing allosteric interactions are not post hoc additions to the model, but rather derived from the microscopic parameters of the Ca^{2+} release site.

Some of these results have previously appeared in abstract form (41).

MODEL FORMULATION

A two-state Ca^{2+}-activated RyR model

Stochastic models of single channel gating often take the form of continuous-time discrete-state Markov chains (for review, see (42,43)). For example, the state-transition diagram for a two-state Ca^{2+}-activated RyR model is defined as

$$(\text{closed})\ \mathcal{C} \underset{k^-}{\overset{k^+ c^\eta}{\rightleftharpoons}} \mathcal{O}\ (\text{open}), \tag{1}$$

where k^+c^η and k^- are transition rates with units of time^{-1}, k^+ is an association rate constant with units $\text{conc}^{-\eta}\,\text{time}^{-1}$, η is the cooperativity of Ca^{2+} binding (usually chosen to be $\eta = 2$), and c is the local $[Ca^{2+}]$. If $c(t)$ is specified, then Eq. 1 defines a discrete-state continuous-time stochastic process, $S(t)$, with the state space $S \in \{\mathcal{C}, \mathcal{O}\}$. When the local $[Ca^{2+}]$ is not time-varying—for example, a fixed background $[Ca^{2+}]$ that we denote as c_∞—then Eq. 1 corresponds to the well-known telegraph process with infinitesimal generator or Q-matrix (42,44) given by

$$Q = q_{ij} = \begin{pmatrix} -k^+ c_\infty^\eta & k^+ c_\infty^\eta \\ k^- & -k^- \end{pmatrix}. \quad (2)$$

Each off-diagonal element of Eq. 2 is the probability per unit time of a transition from state i to state j,

$$q_{ij} = \lim_{\Delta t \to 0} \frac{P\{S(t+\Delta t) = S_j | S(t) = S_i\}}{\Delta t} \quad (i \neq j),$$

and the diagonal elements are selected to ensure that the row sums of Q are zero ($\sum_j q_{ij} = 0$). This condition ensures conservation of probability ($\sum_j p_{ij} = 1$), where

$$p_{ij}(t) = [e^{tQ}]_{ij} = P\{S(t) = S_j | S(0) = S_i\} \quad (t \geq 0)$$

is the element in the i^{th} row and j^{th} column of the matrix exponential. For example, during a small time step Δt, the probability that a channel initially in state i makes a transition into state j is approximated by $p_{ij} \approx [I + Q\Delta t]_{ij}$, and in this case it is clear that $\sum_j q_{ij} = 0$ is required for $\sum_j p_{ij} = 1$. Note that all of the statistical properties of the two-state channel model diagrammed in Eq. 1 can be calculated from the Q-matrix (Eq. 2), and that this matrix can be decomposed as

$$Q = K^- + c_\infty^\eta K^+, \quad (3)$$

where the matrices

$$K^- = \begin{pmatrix} 0 & 0 \\ k^- & -k^- \end{pmatrix} \quad \text{and} \quad K^+ = \begin{pmatrix} -k^+ & k^+ \\ 0 & 0 \end{pmatrix}$$

collect the dissociation and association rate constants, respectively.

Collective gating of RyR clusters

In a natural extension of the single channel modeling approach, a model Ca^{2+} release site composed of N channels is the vector-valued Markov chain, $\mathbf{S}(t) = \{S_1(t), S_2(t), \ldots, S_N(t)\}$, where $S_n(t)$ is the state of channel n at time t (45). We will denote release site configurations as a vector $\boldsymbol{i} = (i_1, i_2, \ldots, i_N)$, where i_n is the state of channel n. The transition rate from release site configuration $\boldsymbol{i}$ to $\boldsymbol{j}$ denoted by q_{ij},

$$(i_1, i_2, \ldots, i_N) \xrightarrow{q_{ij}} (j_1, j_2, \ldots, j_N), \quad (4)$$

is nonzero if the origin ($\boldsymbol{i}$) and destination ($\boldsymbol{j}$) release site configurations are identical with the exception of one channel—that is, $i_n = j_n$ for all $n \neq n'$ where $1 \leq n'(\boldsymbol{i}, \boldsymbol{j}) \leq N$ is the index of the channel changing state—and the $i_{n'} \to j_{n'}$ transition is included in the single-channel model.

More formally, the transition rates q_{ij} for a release site composed of N identical Ca^{2+}-regulated channels (Eq. 2) are given by

$$q_{ij} = \begin{cases} \bar{q}_{ij} & \text{if} \quad \boldsymbol{i} = (i_1, i_2, \ldots, i_{n'-1}, i_{n'}, i_{n'+1}, \ldots, i_N) \quad \text{and} \\ & \quad \boldsymbol{j} = (i_1, i_2, \ldots, i_{n'-1}, j_{n'}, i_{n'+1}, \ldots, i_N) \\ 0 & \text{otherwise} \end{cases}, \quad (5a)$$

$$\bar{q}_{ij} = K^-[i_{n'}, j_{n'}] + K^+[i_{n'}, j_{n'}] c(\boldsymbol{i}, \boldsymbol{j})^\eta, \quad (5b)$$

where either $K^-[i_{n'}, j_{n'}]$ or $K^+[i_{n'}, j_{n'}]$ is the rate constant for the transition being made (only one of which is nonzero) and $c(\boldsymbol{i}, \boldsymbol{j})$ is the relevant [Ca^{2+}], that is, the concentration experienced by channel $n'(\boldsymbol{i}, \boldsymbol{j})$ in the origin configuration $\boldsymbol{i}$. In the following section, we show how $c(\boldsymbol{i}, \boldsymbol{j})$ depends on the mathematical representation of the release site ultrastructure and buffered Ca^{2+} diffusion.

Although it may not be practical to do so for large release sites, the infinitesimal generator matrix, $Q = (q_{ij})$, for a model Ca^{2+} release site can be constructed by enumerating transition rates according to Eq. 5 and selecting the diagonal elements q_{ii} to ensure the rows sum to zero.

Release site ultrastructure and the Ca^{2+} microdomain

Because Ca^{2+}-activated RyRs experience coupling mediated by the buffered diffusion of intracellular Ca^{2+}, the model includes a mathematical representation for the landscape of local [Ca^{2+}] near the Ca^{2+} release site (the so-called Ca^{2+} microdomain) required to specify $c(\boldsymbol{i}, \boldsymbol{j})$ in Eq. 5b. For simplicity, we assume channels are instantaneously coupled via the Ca^{2+} microdomain (30,31)—that is, the formation and collapse of the local peaks in the Ca^{2+} profile are fast compared to the closed and open dwell times of the channels—and we assume the validity of linearly superposing local [Ca^{2+}] increases due to individual channels at the release site (25,27). We also assume that all channels are localized on a planar section of SR membrane ($z = 0$) so that the position of the pore of channel n can be written as $\mathbf{r}_n = x_n\hat{x} + y_n\hat{y}$.

Assuming a single high concentration Ca^{2+} buffer and using the steady-state solution of the linearized equations for the buffered diffusion of intracellular Ca^{2+} (25,26), the increase in [Ca^{2+}] above background at position $\mathbf{r} = x\hat{x} + y\hat{y} + z\hat{z}$ is given by

$$c(\boldsymbol{r}) = \sum_{n=1}^{N} \frac{\sigma_n}{2\pi|\boldsymbol{r}_n - \boldsymbol{r}|(D_c + \kappa_\infty D_b)} \left[1 + \frac{\kappa_\infty D_b}{D_c} \exp\frac{-|\boldsymbol{r}_n - \boldsymbol{r}|}{\lambda}\right], \quad (6a)$$

where

$$\frac{1}{\lambda^2} = \frac{1}{\tau}\left(\frac{1}{D_b} + \frac{\kappa_\infty}{D_c}\right) \quad (6b)$$

$$\frac{1}{\tau} = k_b^+ c_\infty + k_b^- \quad (6c)$$

and

$$\kappa_\infty = \frac{K_b [B]_T}{(K_b + c_\infty)^2}. \quad (6d)$$

In these equations, the sum is over all channels at the release site, σ_n is the source amplitude of channel n (number of Ca^{2+} ions per unit time); D_c and D_b are the diffusion coefficients

for free Ca^{2+} and the Ca^{2+} buffer, respectively; k_b^+ is the buffer association rate constant; k_b^- is the buffer dissociation rate constant, $K_b = k_b^-/k_b^+$; and $[B]_T$ is the total concentration of the Ca^{2+} buffer. Assuming all RyRs have identical source amplitudes,

$$\sigma_n(t) = \begin{cases} 0 & \text{if channel } n \text{ is closed,} \\ \bar{\sigma} & \text{if channel } n \text{ is open,} \end{cases} \tag{7a}$$

and

$$\bar{\sigma} = \frac{i_{Ca}}{2F}, \tag{7b}$$

where i_{Ca} is the unitary current of each channel, 2 is the valence of Ca^{2+}, and F is Faraday's constant.

While Eqs. 6 and 7 define the $[Ca^{2+}]$ at any position $\mathbf{r}$ for a given release site ultrastructure, $\{\mathbf{r}_n\}$, it is helpful to summarize channel-to-channel Ca^{2+} interactions using an $N \times N$ coupling matrix $C = (c_{nm})$ that provides the increase in $[Ca^{2+}]$ over the background (c_∞) experienced by channel m when channel n is open. If $\mathbf{a}_m = x_m\hat{x} + y_m\hat{y} + r_d\hat{z}$ specifies the position of the Ca^{2+} regulatory site for channel m located a small distance r_d above the channel pore, then

$$c_{nm} = \frac{\sigma_O}{2\pi|\boldsymbol{r}_n - \boldsymbol{a}_m|(D_c + \kappa_\infty D_b)}\left[1 + \frac{\kappa_\infty D_b}{D_c}\exp\frac{-|\boldsymbol{r}_n - \boldsymbol{a}_m|}{\lambda}\right]. \tag{8}$$

Using this expression we can determine the Ca^{2+} concentrations needed to specify the rates of Ca^{2+}-mediated transitions in Eqs. 5a and 5b, that is,

$$c(\boldsymbol{i},\boldsymbol{j}) = c_\infty + \sum_{n=1}^{N} \bar{c}_{nn'}, \tag{9a}$$

where

$$\bar{c}_{nn'} = \begin{cases} c_{nn'} & \text{if } i_n \text{ is open,} \\ 0 & \text{otherwise,} \end{cases} \tag{9b}$$

$n'(\boldsymbol{i},\boldsymbol{j})$ is the index of the channel changing state, and i_n is the state of channel n.

Fig. 2 *A* uses Eqs. 6 and 7 and calmodulin-like buffer parameters (see Table 1) to calculate the Ca^{2+} microdomain near a cluster of $N = 25$ open RyRs organized on a Cartesian lattice (Fig. 1 *B*). The strength of Ca^{2+} interactions at the release site can be modified by changing any of the parameters in Eqs. 6 and 7, including the channel source amplitude, buffer parameters, or the diffusion constant for free Ca^{2+}. For example, Fig. 2 *B* shows that increasing the total buffer concentration ($[B]_T$) decreases the local $[Ca^{2+}]$ experienced by the RyRs. Similarly, Fig. 2 *C* shows that the Ca^{2+} coupling strength defined as the average of the off-diagonal elements of the coupling matrix,

$$c_* = \frac{1}{N(N-1)}\sum_{\substack{n,m=1 \\ n\neq m}}^{N} c_{nm}, \tag{10}$$

is a decreasing function of the total buffer concentration $[B]_T$ for any fixed unitary current i_{Ca} and an increasing function of i_{Ca} for any fixed $[B]_T$. Note that the unitary current of RyRs in vivo has been estimated to be <0.6 pA and as low as 0.07 pA in the presence of physiological concentrations of Mg^{2+} (46–48). Because the model does not explicitly include localized depletion of luminal Ca^{2+}, a phenomenon that is expected to reduce the effective unitary current of RyRs in vivo, our standard parameter set includes a unitary current of 0.04 pA (see Table 1).

Allosteric interactions between physically coupled channels

Following the methodology presented in Stern et al. (36), the RyR cluster model with Ca^{2+}-mediated coupling is extended to include allosteric interactions between neighboring channels. We begin by defining dimensionless free energies of interaction ε_{ij} (units of k_BT) that specify the change in free energy experienced by a channel in state j when allosterically coupled to a channel in state i. For convenience we collect these interaction energies in an $M \times M$ matrix $\mathcal{E}$ where M is the number of states in the single-channel model and $\varepsilon_{ij} = \varepsilon_{ji}$ ($i \neq j$) to satisfy the requirement of thermodynamic reversibility. For the two-state single-channel model considered in this article,

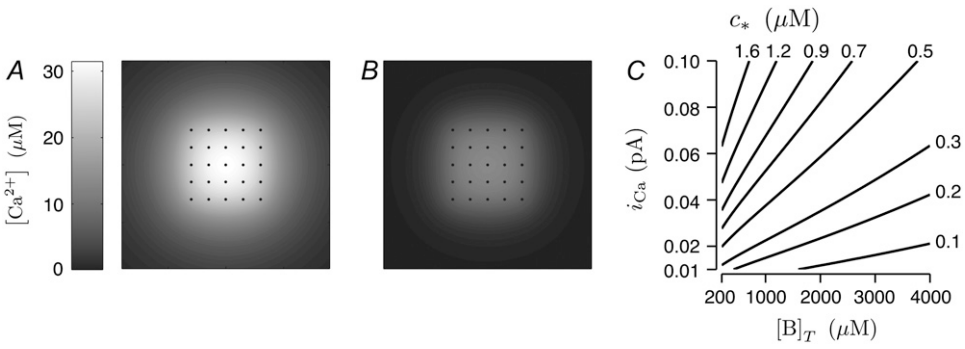

FIGURE 2 (*A* and *B*) The linearized equations for the buffered diffusion of Ca^{2+} (Eqs. 6a–7b) give the steady-state $[Ca^{2+}]$ near ($z = r_d = 30$ nm) a 360 × 360 nm section of planar SR membrane for a cluster of 25 open RyRs (*solid dots*) organized on a Cartesian lattice with interchannel spacing of 30 nm (see Fig. 1 *B*). Individual channels have an effective unitary current of $i_{Ca} = 0.04$ pA and the background $[Ca^{2+}]$ is $c_\infty = 0.1$ μM, while the total Ca^{2+} buffer concentration is (*A*) $[B]_T = 300$ μM or (*B*) $[B]_T = 2000$ μM and buffer parameters are as in Table 1. (*C*) Isoclines showing the average Ca^{2+} coupling strength (c_*) are plotted against $[B]_T$ and the effective unitary current of channels (i_{Ca}) for the 25 channel Ca^{2+} release site shown in *A* and *B*.

TABLE 1 Default parameters used in Ca^{2+} release site simulations for both the full model and the mean-field reduction (when applicable)

Parameter	Value	Unit	Description
Single channel parameters			
k^+	0.04	$\mu M^{-\eta} ms^{-1}$	Association rate constant
k^-	1	ms^{-1}	Dissociation rate constant
c_∞	0.1	μM	Background $[Ca^{2+}]$
η	2		Cooperativity of Ca^{2+} binding
i_{Ca}	0.04	pA	Effective unitary current
r_d	30	nm	Pore to regulatory site distance
Buffer parameters			
k_b^+	100	$\mu M^{-1}\ s^{-1}$	Association rate constant
k_b^-	38	s^{-1}	Dissociation rate constant
D_c	250	$\mu m^2\ s^{-1}$	Ca^{2+} diffusion coefficient
D_b	32	$\mu m^2\ s^{-1}$	Buffer diffusion coefficient

Single-channel kinetic parameters are selected for a dissociation constant or $K_d = 5\ \mu M$ (70). Buffer parameters correspond to calmodulin (27,82). Although the exact location of the Ca^{2+}-regulatory site is unknown, the pore-to-regulatory site distance is consistent with cryo-electron microscopy data that suggests the RyR oligomer has a large $29 \times 29 \times 12$ nm cytoplasmic assembly and a transmembrane assembly that protrudes 7 nm from the center of the cytoplasmic assembly (16,83).

$$\mathcal{E} = \begin{pmatrix} \varepsilon_{\mathcal{CC}} & \varepsilon_{\mathcal{CO}} \\ \varepsilon_{\mathcal{OC}} & \varepsilon_{\mathcal{OO}} \end{pmatrix}, \tag{11}$$

where $\varepsilon_{\mathcal{CO}} = \varepsilon_{\mathcal{OC}}$. Because allosteric interactions require physical contact between neighboring RyRs, the model formulation includes a symmetric $N \times N$ adjacency matrix defined as

$$A = (a_{nm}) = \begin{cases} 1 & \text{if channel } n \text{ and } m \text{ are neighbors,} \\ 0 & \text{otherwise,} \end{cases} \tag{12}$$

where $a_{nn} = 0$ because channels do not experience allosteric interactions with themselves. The nonzero elements of A are chosen consistent with release site ultrastructure (e.g., *dotted lines* in Fig. 1 *B*).

To include the effect of allosteric coupling in the Ca^{2+} release site model, the total allosteric energy experienced by channel $n'(\boldsymbol{i},\boldsymbol{j})$ in the origin and destination configurations of an $\boldsymbol{i} \to \boldsymbol{j}$ transition are calculated as

$$\gamma_i = \sum_{n=1}^{N} a_{nn'} \varepsilon_{i_n i_{n'}} \quad \text{and} \quad \gamma_j = \sum_{n=1}^{N} a_{nn'} \varepsilon_{j_n j_{n'}}, \tag{13}$$

where the sum is over all N channels, $a_{nn'}$ are elements of A, and $\varepsilon_{i_n i_{n'}}$ and $\varepsilon_{j_n j_{n'}}$ are entries of $\mathcal{E}$. The difference between these total allosteric energies $(\gamma_j - \gamma_i)$ is used to modify the equilibrium constant of the $\boldsymbol{i} \to \boldsymbol{j}$ transition, that is,

$$\frac{q_{ij}}{q_{ji}} = \frac{\tilde{q}_{ij}}{\tilde{q}_{ji}} \exp\left[-(\gamma_j - \gamma_i)\right], \tag{14a}$$

$$q_{ij} = \tilde{q}_{ij} \exp\left[-\nu_{ij}(\gamma_j - \gamma_i)\right], \tag{14b}$$

and

$$q_{ji} = \tilde{q}_{ji} \exp\left[-\nu_{ji}(\gamma_i - \gamma_j)\right], \tag{14c}$$

where $\tilde{q}_{ij}$ and $\tilde{q}_{ji}$ denote unmodified rates calculated using Eq. 5 and the parameters $0 \le \nu_{ij} \le 1$ and $\nu_{ji} = 1 - \nu_{ij}$ (36) partition contributions due to allosteric coupling between the forward (q_{ij}) and reverse (q_{ji}) rates. While ν_{ij} and ν_{ji} can potentially have different values for every transition $\boldsymbol{i} \to \boldsymbol{j}$, we assume transition rates involving the association of Ca^{2+} are diffusion-limited. Thus, transition rates for release site configuration changes where channels make $\mathcal{C} \to \mathcal{O}$ transitions are assigned $\nu = 0$. Conversely, $\nu = 1$ for all other configuration changes where channels make $\mathcal{O} \to \mathcal{C}$ transitions.

RESULTS

Ca^{2+} and allosteric coupling at a three RyR cluster

To clarify the model formulation, transition rate expressions corresponding to the example configuration changes shown in Fig. 3 *A* are written below. These configuration changes involve a triangular cluster of three two-state RyRs experiencing Ca^{2+} coupling and nearest-neighbor allosteric interactions. The corresponding Ca^{2+} coupling matrix and allosteric adjacency matrix are

$$C = \begin{pmatrix} c_{11} & c_{12} & c_{13} \\ c_{21} & c_{22} & c_{23} \\ c_{31} & c_{32} & c_{33} \end{pmatrix} \quad \text{and} \quad A = \begin{pmatrix} 0 & 1 & 1 \\ 1 & 0 & 1 \\ 1 & 1 & 0 \end{pmatrix}, \tag{15}$$

respectively, where the c_{nm} are determined using Eq. 8. In each panel of Fig. 3 *A*, the total allosteric energy experienced by the RyR changing state (labeled with *asterisks*) is calculated for both the origin $(\boldsymbol{i})$ and destination $(\boldsymbol{j})$ configurations using Eq. 13.

The $\boldsymbol{i} \to \boldsymbol{j}$ configuration changes shown in Fig. 3 *A* each involve an RyR making a Ca^{2+}-mediated $\mathcal{C} \to \mathcal{O}$ transition (see Eq. 1) at rate q_{ij} that is a function of $c(\boldsymbol{i},\boldsymbol{j})$, that is, the $[Ca^{2+}]$ experienced by the channels changing state (Eq. 9). Let us number the RyRs in a counterclockwise fashion beginning with the channel changing state. For the $\mathcal{CCC} \to \mathcal{OCC}$ configuration change shown in Fig. 3 *A*a, $c(\boldsymbol{i},\boldsymbol{j}) = c_\infty$ because all channels are closed in the origin configuration $\mathcal{CCC}$. For the $\mathcal{CCO} \to \mathcal{OCO}$ configuration change, $c(\boldsymbol{i},\boldsymbol{j}) = c_\infty + c_{31}$ because channel 3 is open in configuration $\mathcal{CCO}$ (Fig. 3 *A*b). Similarly, for the $\mathcal{COO} \to \mathcal{OOO}$ configuration change, $c(\boldsymbol{i},\boldsymbol{j}) = c_\infty + c_{21} + c_{31}$ (Fig. 3 *A*c). Having determined the appropriate $[Ca^{2+}]$ concentrations, Eq. 5b is needed to calculate the transition rates:

$$q_{\mathcal{CCC},\mathcal{OCC}} = k^+ c_\infty^\eta, \tag{16a}$$

$$q_{\mathcal{CCO},\mathcal{OCO}} = k^+ (c_\infty + c_{31})^\eta, \tag{16b}$$

and

$$q_{\mathcal{COO},\mathcal{OOO}} = k^+ (c_\infty + c_{21} + c_{31})^\eta. \tag{16c}$$

Because it is assumed that configuration changes involving the binding of Ca^{2+} are diffusion limited, these rates are not modified due to allosteric interactions (i.e., $\nu_{ij} = 0$).

Conversely, $\boldsymbol{j} \to \boldsymbol{i}$ configuration changes shown in Fig. 3 *A* involve channels making unimolecular $\mathcal{O} \to \mathcal{C}$ transitions

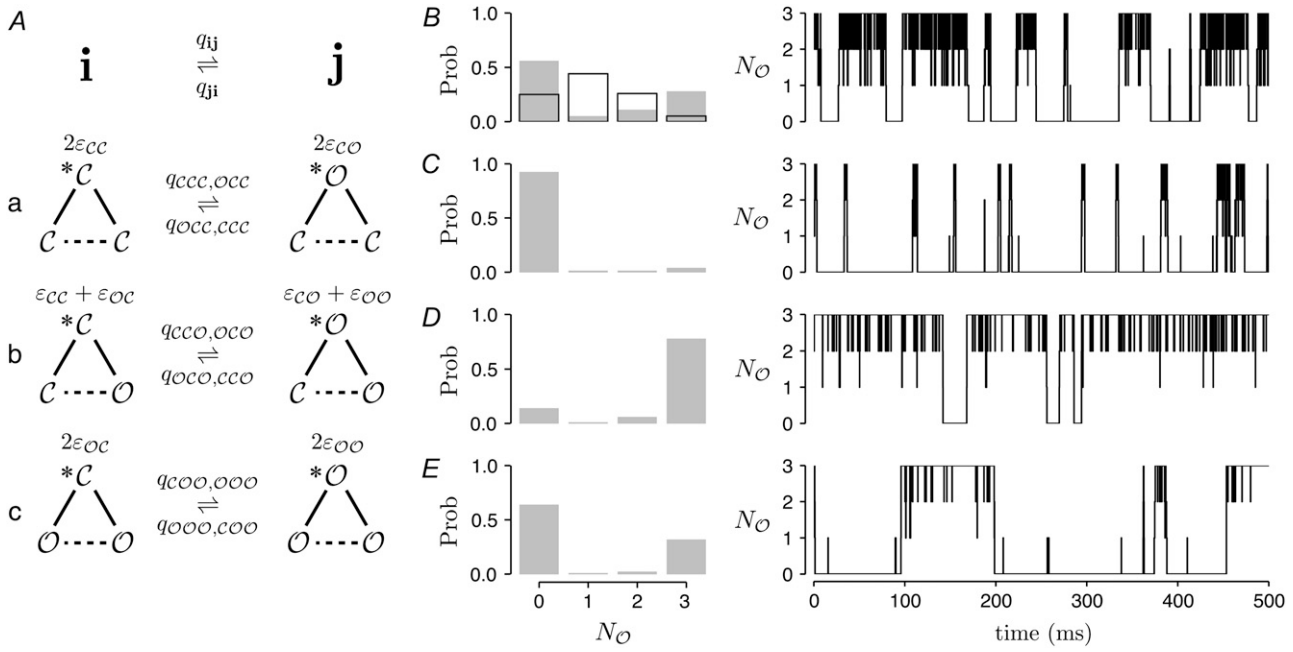

FIGURE 3 (*A*) Example configuration changes involving three two-state RyRs with pore-to-pore interchannel spacing of 30 nm. Allosteric interactions are indicated by solid and dashed lines. Transition rates depend on the allosteric interactions of the channel changing state (*solid lines*) shown above each configuration. (*B*) RyR collective gating when channels experience coupling via the Ca^{2+} microdomain ($[B]_T = 3566\ \mu M$, $c_* = 0.75\ \mu M$) but no allosteric interactions $\varepsilon_{CC} = \varepsilon_{OO} = 0$. Shaded bars show the steady-state probability distribution for the number of open channels N_O at the release site. Open bars give the binomial distribution with the same mean as shaded bars; the difference shows that channels do not gate independently. (*C–E*) RyR collective gating. In addition to Ca^{2+} coupling ($c_* = 0.75\ \mu M$), channels experience allosteric interactions that stabilize closed channel pairs (*C*, $\varepsilon_{CC} = -0.8$, $\varepsilon_{OO} = 0$) open channel pairs (*D*, $\varepsilon_{CC} = 0$, $\varepsilon_{OO} = -0.8$) or both in a balanced fashion (*E*, $\varepsilon_{CC} = \varepsilon_{OO} = -0.8$) Parameters: $k^+ = 1.5\ \mu M^{-\eta}\ ms^{-1}$, $k^- = 0.5\ ms^{-1}$, and as in Table 1.

at the base rate $q_{ji} = k^-$ that is modified by the change in allosteric interaction energy experienced by the channel changing state. Using $\nu_{ji} = 1$, the rates for $\boldsymbol{j} \rightarrow \boldsymbol{i}$ configuration changes are given by (Eq. 14c)

$$q_{OCC,CCC} = k^- \exp[-2(\varepsilon_{CC} - \varepsilon_{CO})], \quad (17a)$$

$$q_{OCO,CCO} = k^- \exp[-((\varepsilon_{CC} - \varepsilon_{CO}) + (\varepsilon_{OC} - \varepsilon_{OO}))], \quad (17b)$$

and

$$q_{OOO,COO} = k^- \exp[-2(\varepsilon_{OC} - \varepsilon_{OO})]. \quad (17c)$$

Note that in these transition rate expressions, the elements of the allosteric interaction energy matrix occur as the differences $\varepsilon_{CC} - \varepsilon_{CO}$ and $\varepsilon_{OC} - \varepsilon_{OO}$. This is true regardless of the number of channels, and we may without loss of generality fix $\varepsilon_{CO} = \varepsilon_{OC} = 0$. That is, we will probe the effects of allosteric interactions on Ca^{2+} release site dynamics by varying only the change in free energy due to allosterically interacting closed-closed (ε_{CC}) and open-open (ε_{OO}) channel pairs. Because we are primarily concerned with the effects of allosteric interactions that promote synchronous gating, we assume allosteric interactions stabilize closed-closed and/or open-open channel pairs (i.e., $\varepsilon_{CC} \leq 0$ and $\varepsilon_{OO} \leq 0$). For simplicity, we focus on three allosteric coupling paradigms in which allosteric interactions stabilize

1. Closed-closed channel pairs ($\varepsilon_{CC} = < 0$, $\varepsilon_{OO} = 0$).
2. Open-open channel pairs ($\varepsilon_{OO} = 0$, $\varepsilon_{OO} < 0$).
3. Both closed-closed and open-open channel pairs in a balanced fashion ($\varepsilon_{OO} = \varepsilon_{OO} < 0$).

The simulations shown in Fig. 3, *B–E*, demonstrate how synchronizing allosteric interactions included in these three ways affect the dynamics of the synchronous gating of the three RyRs. Simulations are carried out using the exact numerical method presented in Appendix A and, for simplicity, the configuration of the RyRs is summarized by plotting only the number of open channels (N_O) as a function of time. Interestingly, Fig. 3 *B* demonstrates that synchronizing allosteric interactions are not required ($\varepsilon_{CC} = \varepsilon_{OO} = 0$) for channels to exhibit synchronous gating. Rather, channels may exhibit coupled gating that is mediated entirely via the buffered diffusion of local Ca^{2+} as long as the average Ca^{2+} coupling strength is sufficient ($c_* = 0.75\ \mu M$) (31). Shaded bars in the left panel of Fig. 3 *B* show the steady-state probability distribution for the number of open RyRs (N_O) directly calculated from the relevant Q-matrix as described in Appendix B. The disagreement between these results and the open bars, showing a binomial distribution with the same mean, is a signature of the cooperative gating of these RyRs.

While Fig. 3 *B* demonstrates that the synchronous gating of channels can be mediated entirely via Ca^{2+}, Fig. 3, *C–E*, show how synchronizing allosteric interactions affect the dynamics of coupled gating. For example, Fig. 3 *C* demonstrates that when closed channel pairs are stabilized ($\varepsilon_{CC} =$

-0.8, $\varepsilon_{\mathcal{OO}} = 0$), the steady-state probability of having zero open channels ($N_{\mathcal{O}} = 0$) increases while the probability of $N_{\mathcal{O}} = 3$ decreases relative to Fig. 3 *B*. Conversely, Fig. 3 *D* illustrates that when allosteric interactions stabilize open channel pairs ($\varepsilon_{\mathcal{CC}} = 0$, $\varepsilon_{\mathcal{OO}} = -0.8$), the probability of having a maximally activated release site ($N_{\mathcal{O}} = 3$) increases. In Fig. 3 *E* allosteric interactions stabilize closed-closed and open-open channel pairs in a balanced fashion ($\varepsilon_{\mathcal{CC}} = \varepsilon_{\mathcal{OO}} = -0.8$) and the probability of both $N_{\mathcal{O}} = 0$ and $N_{\mathcal{O}} = 3$ increases while the probability of $N_{\mathcal{O}} = 1$ and $N_{\mathcal{O}} = 2$ decreases compared to Fig. 3 *B*.

Effects of Ca^{2+} and allosteric coupling strength on spontaneous sparks

The previous section demonstrated how the dynamics of coupled RyR gating may depend on synchronizing allosteric interactions that stabilize closed channel pairs, open channel pairs, or both in a balanced fashion. In this section, release sites composed of 25 nearest-neighbor coupled RyRs organized on a Cartesian lattice (see Fig. 1 *B*) are used to investigate how Ca^{2+} spark generation and termination depend on both the strength of coupling mediated by the Ca^{2+} microdomain and the strength of synchronizing allosteric interactions introduced in one of these three ways. Note that nearest-neighbor coupling implies that each channel experiences allosteric interactions with 2–4 other channels, while increases in the Ca^{2+} microdomain due to open RyRs are experienced by all channels.

Fig. 4 *A* shows a simulation in which the strength of allosteric interactions ($\varepsilon_{\mathcal{CC}} = -0.2$, $\varepsilon_{\mathcal{OO}} = 0$) and Ca^{2+} coupling ($c_* = 0.55$ μM) are selected to illustrate the phenomenon of stochastic Ca^{2+} excitability reminiscent of spontaneous Ca^{2+} sparks. While the channels at the release site are closed most of the time ($N_{\mathcal{O}} < 5$), on occasion the RyRs simultaneously open ($N_{\mathcal{O}} \approx 25$). Fig. 5 shows that the sparks observed in Fig. 4 *A* are sensitive to changes in the strength of allosteric interactions that stabilize closed channel pairs. For example, the release site is tonically active when allosteric interactions are not included in simulations ($\varepsilon_{\mathcal{CC}} = \varepsilon_{\mathcal{OO}} = 0$, Fig. 5 *A*). On the other hand, sparks fail to initiate when the strength of allosteric interactions that stabilize closed channel pairs is greater than in Fig. 4 *A* ($\varepsilon_{\mathcal{CC}} = -0.4$, $\varepsilon_{\mathcal{OO}} = 0$, Fig. 5 *B*).

A response measure that is strongly correlated with the presence of sparks in Monte Carlo simulations is the so-called Ca^{2+} spark *Score* introduced in (31). The *Score* is defined as the index of dispersion of the fraction of open channels ($f_O = N_{\mathcal{O}}/N$) and is given by

$$Score = \frac{\mathrm{Var}[f_O]}{E[f_O]} = \frac{1}{N}\frac{\mathrm{Var}[N_{\mathcal{O}}]}{E[N_{\mathcal{O}}]}. \tag{18}$$

Score values >0.3 are indicative of spark-like excitability in stochastic Ca^{2+} release site simulations (30,31). For example, using the observed probability distribution for the number of open channels at the release site estimated from a long Monte Carlo simulation as described in Appendix B (Fig.

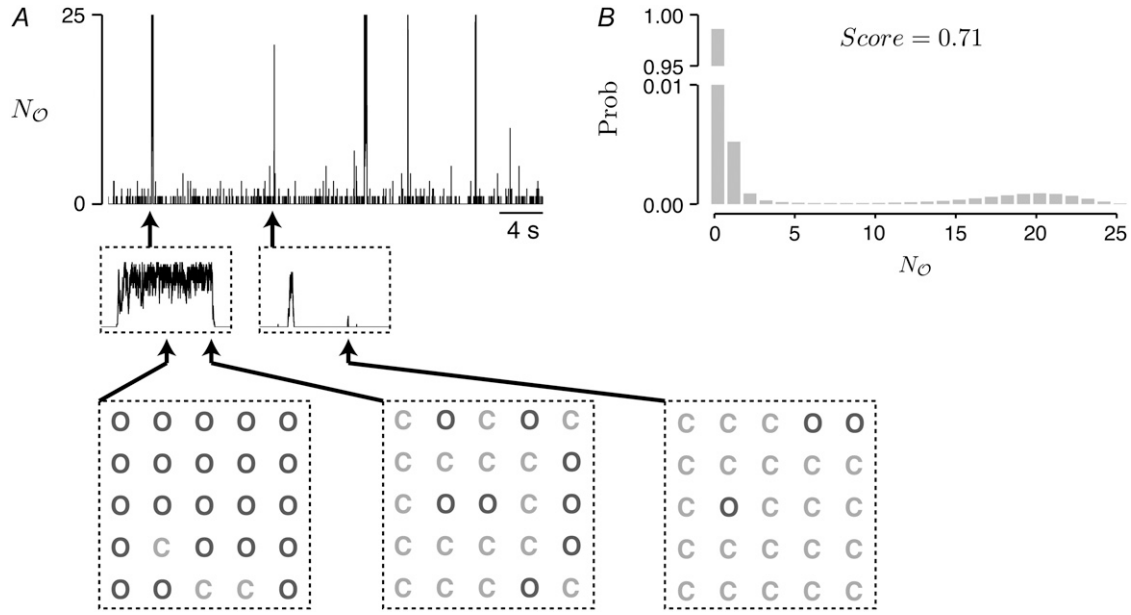

FIGURE 4 (*A*) Ca^{2+} release site simulation involving 25 RyRs organized on a Cartesian lattice exhibits stochastic Ca^{2+} excitability reminiscent of spontaneous sparks when channels experience coupling via increases in the local $[Ca^{2+}]$ ($[B]_T = 937.5$ μM, $c_* = 0.55$ μM) and nearest-neighbor allosteric interactions that stabilize closed channel pairs ($\varepsilon_{\mathcal{CC}} = -0.2$, $\varepsilon_{\mathcal{OO}} = 0$). Insets expand 50 ms of the simulation beginning at the times indicated by arrows and show snapshots giving the states of all 25 RyRs at the release site. (*B*) The Ca^{2+} spark *Score* corresponding to the simulation is calculated using Eq. 18 and the steady-state probability distribution for the number of open channels ($N_{\mathcal{O}}$) at the release site (*right panel*) estimated from a long (>20 s) Monte Carlo simulation as described in Appendix B. Parameters as in Table 1.

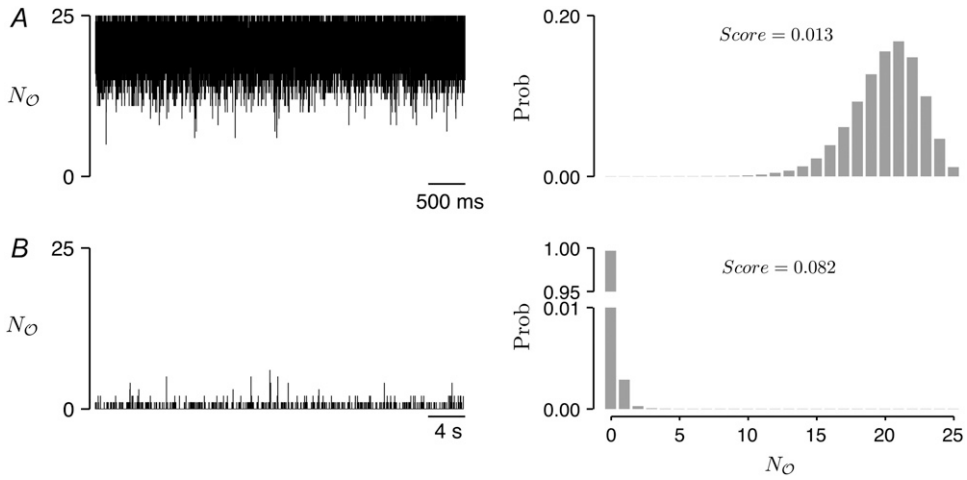

FIGURE 5 Ca^{2+} sparks exhibited in Fig. 4 are sensitive to changes in the strength of allosteric interactions that stabilize closed channel pairs only when the strength of Ca^{2+} interactions is fixed ($c_* = 0.55\ \mu$M). (*A*) Sparks fail to terminate when allosteric interactions are not included ($\varepsilon_{\mathcal{CC}} = 0$, $\varepsilon_{\mathcal{OO}} = 0$). (*B*) Sparks fail to initiate when the strength of allosteric interactions that stabilize closed channel pairs is increased ($\varepsilon_{\mathcal{CC}} = -0.4$, $\varepsilon_{\mathcal{OO}} = 0$). Histograms for the number of open channels shown in *right panels* (see Fig. 4) are used to calculate the *Score* of each simulation. Parameters as in Table 1.

4 *B*), the *Score* corresponding to the simulation shown in Fig. 4 is a high value of 0.71. Conversely, the tonically active release site shown in Fig. 5 *A* has a low *Score* of 0.013 because $E[N_{\mathcal{O}}]$ is large. The quiescent release site shown in Fig. 5 *B* also has a low *Score* of 0.082.

While Figs. 4 and 5 demonstrated that Ca^{2+} sparks are sensitive to changes in the strength of allosteric interactions that stabilize closed channel pairs, Fig. 6 *A* shows that sparks observed in simulations of a 25 RyR release site are also sensitive to the Ca^{2+} coupling strength. For example, triangles show the *Score* (reported as the mean ± SD of 10 Monte Carlo simulations) as a function of c_* when the strength of allosteric interactions that stabilize closed channel pairs is $\varepsilon_{\mathcal{CC}} = -0.2$ as in Fig. 4. The Ca^{2+} coupling strength (c_*) is systematically varied by increasing or decreasing the total buffer concentration ($[B]_T$). Note that sparks are observed in simulations (*Score* > 0.3) over a range of Ca^{2+} coupling strengths but are not observed (*Score* < 0.3) in simulations that use $c_* < 0.4\ \mu$M because the Ca^{2+} coupling strength is insufficient to initiate sparks. Similarly, *Score* < 0.3 when $c_* > 0.7\ \mu$M because the Ca^{2+} coupling strength is too large to allow spark termination. Fig. 6 *A* also shows that the optimal Ca^{2+} coupling strength—that is, the c_* resulting in the highest *Score*—is sensitive to the strength of allosteric interactions that stabilize closed channels. Indeed, comparing circles ($\varepsilon_{\mathcal{CC}} = 0$) and squares ($\varepsilon_{\mathcal{CC}} = -0.4$) to triangles ($\varepsilon_{\mathcal{CC}} = -0.2$), we notice that the optimal c_* is an increasing function of the magnitude of $\varepsilon_{\mathcal{CC}}$. In comparison, Fig. 6 *B* demonstrates that as the strength of allosteric interactions that stabilize open channel pairs increases, the optimal c_* decreases. On the other hand, Fig. 6 *C* shows that increasing the strength of allosteric interactions that stabilize both closed-closed and open-open channel pairs in a balanced fashion has little effect on the optimal value of c_*.

Fig. 6 demonstrates that sparks depend on c_*, $\varepsilon_{\mathcal{OO}}$, and $\varepsilon_{\mathcal{CC}}$ in a complicated manner. For example, sparks that are eliminated as c_* increases may be recovered by increasing the strength of allosteric interactions that stabilize closed channel pairs ($\varepsilon_{\mathcal{CC}}$) or by decreasing the strength of allosteric interactions that stabilize open channel pairs ($\varepsilon_{\mathcal{OO}}$). On the other hand, sparks that are eliminated as c_* decreases may be recovered by decreasing the magnitude of $\varepsilon_{\mathcal{CC}}$ or increasing the magnitude of $\varepsilon_{\mathcal{OO}}$. Note that for all three types of allosteric interactions there are Ca^{2+} coupling strengths (c_*) for which stronger interactions lead to more robust sparks. Indeed, summary plots in Fig. 7 *A* show that the *Score* at these optimal c_* values is a monotonically increasing function of the strength of allosteric interactions. Interestingly, the *Score* is enhanced the most when both closed-closed and open-open channel pairs are increasingly stabilized in a balanced fashion (*circles*).

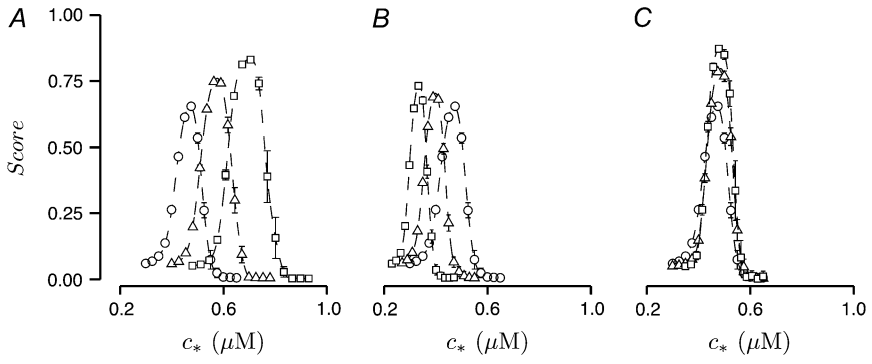

FIGURE 6 (*A–C*) The Ca^{2+} spark *Score* (mean ± SD of 10 long (>20 s) Monte Carlo simulations involving 25 RyRs organized on a Cartesian lattice with random initial conditions) as a function of the Ca^{2+} coupling strength (c_*) and the strength of nearest-neighbor allosteric interactions that stabilize closed channel pairs (*A*) $\varepsilon_{\mathcal{OO}} = 0$ and $\varepsilon_{\mathcal{CC}} = 0$ (*circles*), $\varepsilon_{\mathcal{CC}} = -0.2$ (*triangles*), or $\varepsilon_{\mathcal{CC}} = -0.4$ (*squares*); open channel pairs (*B*) $\varepsilon_{\mathcal{CC}} = 0$ and $\varepsilon_{\mathcal{OO}} = 0$ (*circles*), $\varepsilon_{\mathcal{OO}} = -0.2$ (*triangles*), or $\varepsilon_{\mathcal{OO}} = -0.4$ (*squares*); or both in a balanced fashion (*C*) $\varepsilon_{\mathcal{CC}} = \varepsilon_{\mathcal{OO}} = 0$ (*circles*), $\varepsilon_{\mathcal{CC}} = \varepsilon_{\mathcal{OO}} = -0.2$ (*triangles*), or $\varepsilon_{\mathcal{CC}} = \varepsilon_{\mathcal{OO}} = -0.4$ (*squares*). Data are interpolated with cubic splines (*dashed lines*) for clarity. Parameters as in Table 1.

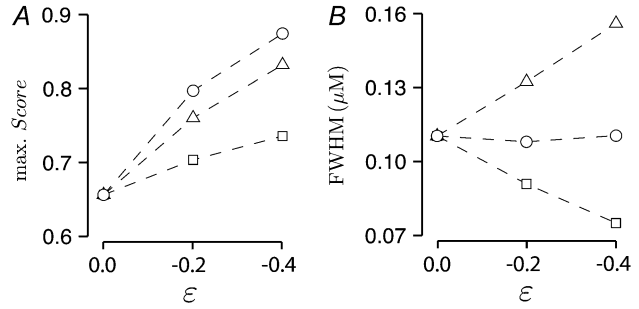

FIGURE 7 (*A*) The *Score* at the optimal c_* (maximum *Score*) and (*B*) the full width at half-maximum (FWHM) of the cubic spline fits of data in Fig. 6 are plotted as a function of the strength of stabilizing allosteric interactions (ε) when allosteric interactions stabilize closed channel pairs (*triangles*, $\varepsilon_{\mathcal{CC}} = \varepsilon$, $\varepsilon_{\mathcal{OO}} = 0$), open channel pairs (*squares*, $\varepsilon_{\mathcal{CC}} = 0$, $\varepsilon_{\mathcal{OO}} = \varepsilon$), or both in a balanced fashion (*circles*, $\varepsilon_{\mathcal{CC}} = \varepsilon_{\mathcal{OO}} = \varepsilon$).

In Fig. 7 *B* the sensitivity of sparks to the Ca^{2+} coupling strength is quantified using the full width at half-maximum (FWHM) of cubic spline fits to the results of Fig. 6 (*dashed lines*); a larger FWHM implies less sensitivity to changes in c_*. The triangles of Fig. 7 *B* show that sparks are less sensitive to variations in c_* as the strength of allosteric interactions that stabilize closed channel pairs increases. Conversely, the squares show that sparks are more sensitive to c_* as the strength of allosteric interactions that stabilize open channel pairs increases. The circles show that increasing the strength of allosteric interactions that stabilize both closed-closed and open-open channel pairs in a balanced fashion has little effect on the FWHM.

The effect of washing out allosteric interactions on spark statistics

In the previous section we showed how the presence or absence of Ca^{2+} sparks depends on both the strength of Ca^{2+} coupling (c_*) and the strength of stabilizing allosteric interactions ($\varepsilon_{\mathcal{CC}}$ and $\varepsilon_{\mathcal{OO}}$). Next, we investigate how spark statistics (duration, interspark interval, and frequency) are affected by washing-out stabilizing allosteric interactions, that is, we study how these spark statistics change as an increasing fraction of nearest-neighbor allosteric couplings are removed. Many experimental studies show that genetic deficiencies in, and the pharmacological washout of, the FK-binding proteins that mediate allosteric interactions lead to cardiac arrhythmias and changes in spark dynamics (49–51). The following simulations aim to clarify how these experimental results may be interpreted as evidence for allosteric interactions that stabilize closed channel pairs, open channel pairs, or both (see Discussion).

The shaded bars in Fig. 8 *A* are probability distributions of spark duration and interspark interval estimated from multiple spark simulations (the mean is indicated by *shaded triangles*). As in Fig. 4, twenty-five RyRs experience nearest-neighbor allosteric interactions that stabilize closed channel pairs ($\varepsilon_{\mathcal{CC}} = -0.2$, $\varepsilon_{\mathcal{OO}} = 0$), and the Ca^{2+} coupling strength is selected to ensure a high *Score* ($c_* = 0.58$ μM). Spark duration is defined as the period beginning when one-fifth of the channels at the release site open ($N_{\mathcal{O}} = 4 \rightarrow 5$) and ending when all channels close ($N_{\mathcal{O}} = 0$), thus excluding small sparks from the calculation. Interspark interval is the

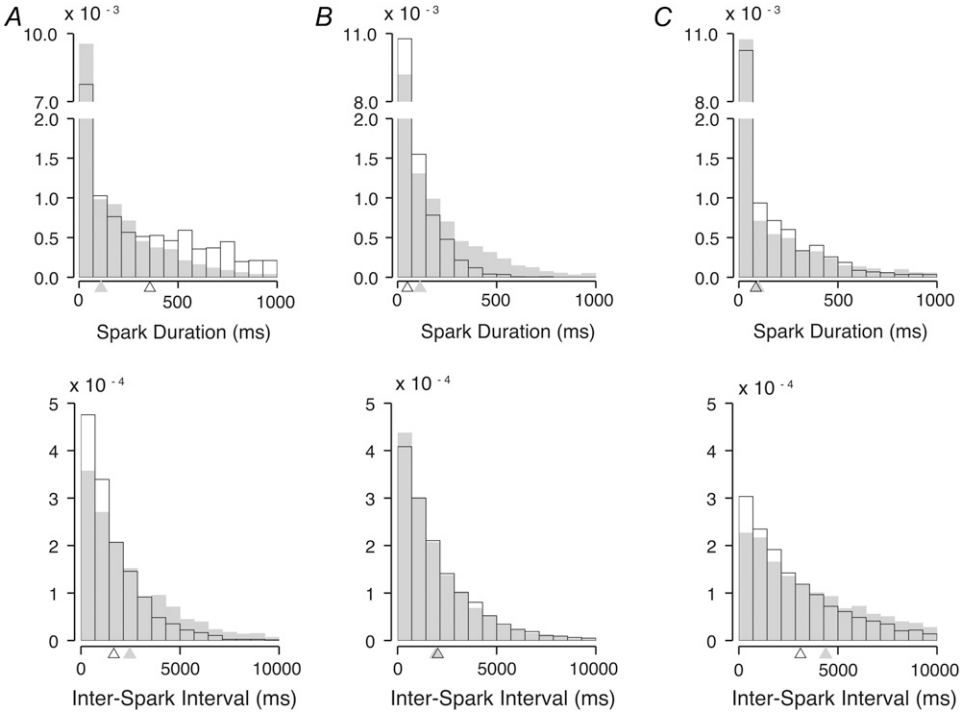

FIGURE 8 Shaded bars are probability distributions of Ca^{2+} spark duration and interspark interval estimated from simulations involving 25 RyRs organized on a Cartesian lattice (means indicated by *shaded triangles*). RyRs experience coupling via the Ca^{2+} microdomain (*A*) $c_* = 0.58$, (*B*) $c_* = 0.40$, and (*C*) $c_* = 0.48$ μM; and nearest-neighbor allosteric interactions that stabilize closed channel pairs (*A*) $\varepsilon_{\mathcal{CC}} = -0.2$, $\varepsilon_{\mathcal{OO}} = 0$; open channel pairs (*B*) $\varepsilon_{\mathcal{CC}} = 0$, $\varepsilon_{\mathcal{OO}} = -0.2$; or both in a balanced fashion (*C*) $\varepsilon_{\mathcal{CC}} = \varepsilon_{\mathcal{OO}} = -0.2$. Open bars (and *triangles*) are spark statistic distributions (and means) calculated when one-fifth of the nearest-neighbor allosteric couplings are selected at random and removed from simulations. Each histogram is calculated using 1200–6333 simulated sparks. Parameters as in Table 1.

time between the end of a spark and the beginning of the subsequent spark.

For comparison, open bars in Fig. 8 *A* are the spark duration and interspark interval distributions after one-fifth of the nearest-neighbor allosteric couplings are selected at random and eliminated from the simulations. Notice that this washout of allosteric interactions that stabilize closed channel pairs has the effect of increasing the expected spark duration and decreasing the expected interspark interval (compare *open* and *shaded triangles*). On the other hand, Fig. 8 *B* shows that when allosteric interactions stabilize open channel pairs ($\varepsilon_{\mathcal{CC}} = 0$, $\varepsilon_{\mathcal{CC}} = -0.2$, and $c_* = 0.40$ μM), removing one-fifth of these couplings decreases the expected spark duration with little change to the interspark interval. When both closed-closed and open-open channel pairs are stabilized in a balanced fashion ($\varepsilon_{\mathcal{CC}} = \varepsilon_{\mathcal{OO}} = -0.2$, $c_* = 0.48$ μM), washout of allosteric couplings decreases interspark interval but has little effect on spark duration (Fig. 8 *C*).

To further probe the effects of washing out allosteric interactions, Fig. 9, *A* and *B*, show the mean and standard deviation of spark duration and interspark interval plotted against the fraction of allosteric couplings removed from simulations (denoted as ϕ). Similar to Fig. 8, allosteric interactions are included to stabilize closed channel pairs (*triangles*), open channel pairs (*squares*), or both in a balanced fashion (*circles*). In each case, the Ca^{2+} coupling strength of $c_* =$ 0.58, 0.40, and 0.48 μM, respectively, is selected to maximize the Ca^{2+} spark *Score* before the washout of synchronizing allosteric interactions ($\phi = 0$); thus, the *Score* is always a decreasing function of ϕ (not shown). When the squares and circles of Fig. 9, *A* and *B*, are recalculated using $c_* = 0.58$ μM, qualitatively similar results are obtained.

The results shown in Fig. 9, *A* and *B*, are consistent with those shown in Fig. 8. When allosteric interactions that stabilize closed channel pairs are washed out (increasing ϕ), spark duration increases and interspark interval decreases (*triangles*). When allosteric interactions that stabilize open channel pairs are washed out, spark duration decreases but interspark interval is largely unchanged (*squares*). When both closed-closed and open-open channel pairs are stabilized in a balanced fashion, washout causes interspark interval to decrease but spark duration is unchanged (*circles*). Notice that the standard deviations (*bars*) of spark statistics are approximately proportional to the means regardless of the degree of washout.

Because the allosteric couplings washed out in the simulations of Fig. 9, *A* and *B*, are randomly selected, there are many realizations of the allosteric adjacency matrix *A* consistent with any nonzero ϕ. To show the effects of variations in allosteric connectivity on spark dynamics, multiple symbols plotted at each value of ϕ show the mean spark duration and interspark interval using different realizations of *A*. The proximity of these symbols to each other at any given value of ϕ indicates that the dynamics of Ca^{2+} sparks—as measured by duration and interspark interval—are largely insensitive to these variations in allosteric connectivity.

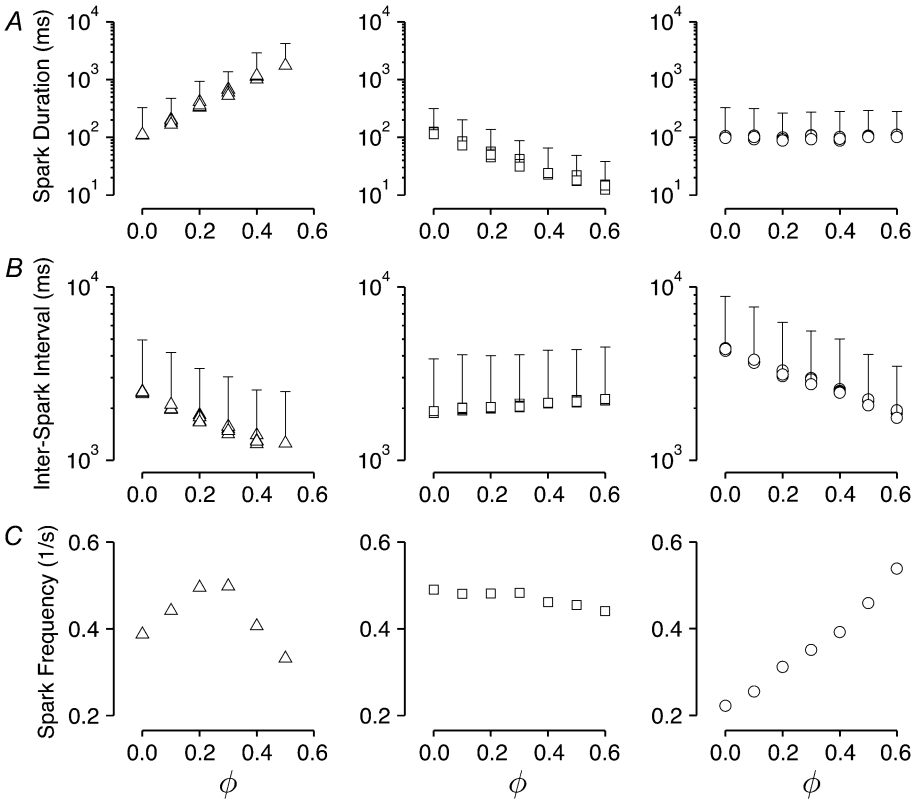

FIGURE 9 (*A* and *B*) The (*A*) Ca^{2+} spark duration and (*B*) interspark interval (mean + SD of distributions such as those in Fig. 8 calculated using 334–14,290 simulated sparks) are plotted against the fraction of allosteric couplings randomly removed from simulations (ϕ). Using parameters identical to Fig. 8 the 25 RyRs experience Ca^{2+} coupling and allosteric interactions that stabilize closed channel pairs (*triangles*), open channel pairs (*squares*), or both in a balanced fashion (*circles*). Multiple symbols at each ϕ show results from simulations that use different realizations of the allosteric adjacency matrix *A* (see text). (*C*) The spark frequency plotted against ϕ is calculated using the data from *A* and *B* that include error bars. Spark statistics are reported at a given value of ϕ only if the Ca^{2+} spark *Score* > 0.3.

Fig. 9 *C* shows the spark frequency—defined as the reciprocal of the sum of the mean spark duration and interspark interval—plotted against ϕ for the three allosteric coupling paradigms. When allosteric interactions that stabilize closed channel pairs are washed out, spark frequency increases but ultimately decreases (*triangles*). When allosteric interactions stabilize open channel pairs (*squares*), spark frequency is a nearly constant function of ϕ. When both closed-closed and open-open channel pairs are stabilized in a balanced fashion, spark frequency increases during washout (*circles*).

A mean-field RyR cluster model

In previous sections, we used Monte Carlo simulations to study how both the strength of Ca^{2+} coupling and stabilizing allosteric interactions contribute to the dynamics of sparks. Much of the complexity of these simulations is due to the spatially explicit account of channel-to-channel coupling represented by the Ca^{2+} coupling matrix C and the allosteric adjacency matrix A. To facilitate parameter studies of the effects of allosteric coupling on spark statistics, this section presents a mean-field approximation applicable to a cluster of two-state RyRs coupled via the buffered diffusion of Ca^{2+} and nearest-neighbor allosteric interactions.

The mean-field approximation is perhaps best introduced by considering a simplified Ca^{2+} coupling matrix that takes the form (31)

$$\overline{C} = \begin{pmatrix} c_{\mathrm{d}} & c_* & \cdots & c_* \\ c_* & c_{\mathrm{d}} & \ddots & \vdots \\ \vdots & \ddots & \ddots & c_* \\ c_* & \cdots & c_* & c_{\mathrm{d}} \end{pmatrix}, \tag{19}$$

where the identical off-diagonal elements (c_*) are the average of the $N(N-1)$ off-diagonal elements of the original Ca^{2+} coupling matrix C (Eq. 10). (The diagonal elements c_{d} that represent domain Ca^{2+} are inconsequential to simulations involving clusters of RyRs with no Ca^{2+}-mediated transition out of an open state.) Consider also an allosteric adjacency matrix that takes a similar simplified form,

$$\overline{A} = \begin{pmatrix} 0 & a_* & \cdots & a_* \\ a_* & 0 & \ddots & \vdots \\ \vdots & \ddots & \ddots & a_* \\ a_* & \cdots & a_* & 0 \end{pmatrix}, \tag{20}$$

where $0 \le a_* \le 1$ is the average allosteric connectivity calculated from the off-diagonal elements of the original allosteric adjacency matrix $A = (a_{\mathrm{nm}})$,

$$a_* = \frac{1}{N(N-1)} \sum_{\mathrm{n}\neq\mathrm{m}} a_{\mathrm{nm}}. \tag{21}$$

Note that it is not possible to choose a release site ultrastructure so that $\overline{C}$ is equal to C with $N > 3$ channels on a planar membrane. Likewise, $\overline{A}$ will not be equal to A unless allosteric coupling is all-to-all, a situation not consistent with RyR clusters in which the extent of interchannel physical coupling is limited to nearest neighbors. Nevertheless, in simulations performed using $\overline{C}$ and $\overline{A}$, the RyRs are indistinguishable and the $[Ca^{2+}]$ and allosteric interaction energy experienced by channels depends only on the number of open and closed RyRs at the release site. Importantly, simulations using $\overline{C}$ and $\overline{A}$ satisfy a lumpability condition that allows all release site configurations with the same number of channels in each state to be agglomerated without further approximation (31,52). This yields a contracted Markov chain with state-transition diagram

$$0 \underset{q_{10}}{\overset{q_{01}}{\rightleftharpoons}} 1 \underset{q_{21}}{\overset{q_{12}}{\rightleftharpoons}} 2 \underset{q_{32}}{\overset{q_{23}}{\rightleftharpoons}} \cdots \underset{q_{\mathrm{N}-1,\mathrm{N}-2}}{\overset{q_{\mathrm{N}-2,\mathrm{N}-1}}{\rightleftharpoons}} N-1 \underset{q_{\mathrm{N},\mathrm{N}-1}}{\overset{q_{\mathrm{N}-1,\mathrm{N}}}{\rightleftharpoons}} N, \tag{22}$$

where the state of the system $S(t) \in \{0, 1, \ldots, N\}$ is the number of open channels $N_{\mathcal{O}}$ at the release site and q_{ij} is the rate of the $N_{\mathcal{O}} = i \rightarrow j$ transition (see below). The number of closed channels is given by $N_{\mathcal{C}} = N - N_{\mathcal{O}}$.

Equation 22 describes a birth-death process with boundaries with skip-free transitions that increase ($N_{\mathcal{O}} = n \rightarrow n+1$) or decrease ($N_{\mathcal{O}} = n \rightarrow n-1$) the number of open channels at the release site. The $N+1$ by $N+1$ generator matrix corresponding to Eq. 22 is tridiagonal,

$$Q = \begin{pmatrix} \diamond & q_{01} & & & & \\ q_{10} & \diamond & q_{12} & & & \\ & q_{21} & \diamond & q_{23} & & \\ & & & \ddots & & \\ & & & q_{\mathrm{n}-1,\mathrm{n}-2} & \diamond & q_{\mathrm{n}-1,\mathrm{n}} \\ & & & & q_{\mathrm{n},\mathrm{n}-1} & \diamond \end{pmatrix}, \tag{23}$$

with diagonal elements ($\diamond$) selected to ensure row sums of zero. The birth rate ($q_{\mathrm{n},\,\mathrm{n}+1}$) for the $n \rightarrow n+1$ transition is given by

$$q_{\mathrm{n},\mathrm{n}+1} = (N-n)k^+(c_\infty + nc_*)^\eta \ (0 \le n \le N-1), \tag{24}$$

where $(N-n)$ is the number of closed channels at the release site that may potentially open and $c_\infty + N_{\mathcal{O}}c_*$ is the $[Ca^{2+}]$ experienced by all RyRs. While our assumption that the binding of Ca^{2+} is diffusion-limited leads to birth rates that are not dependent on allosteric energies, the death rates are modified due to allosteric interactions and are given by

$$q_{\mathrm{n},\mathrm{n}-1} = nk^-\exp\{-a_*[(n-1)(\varepsilon_{\mathcal{OC}} - \varepsilon_{\mathcal{OO}}) + (N-n)(\varepsilon_{\mathcal{CC}} - \varepsilon_{\mathcal{CO}})]\} \ (1 \le n \le N), \tag{25}$$

where n is the number of open channels at the release site that may potentially close, the coefficients $(n-1)$ and $(N-n)$ are the number of open and closed neighbors, and $\varepsilon_{\mathcal{OC}} - \varepsilon_{\mathcal{OO}}$ and $\varepsilon_{\mathcal{CC}} - \varepsilon_{\mathcal{CO}}$ are the differences in free energies experienced by a transitioning channel due to allosteric couplings with neighboring open and closed channels. Because we have without loss of generality set $\varepsilon_{\mathcal{CO}} = \varepsilon_{\mathcal{OC}} = 0$, Eq. 25 simplifies to

$$q_{\mathrm{n},\mathrm{n}-1} = nk^-\exp\{-a_*[(N-n)\varepsilon_{\mathcal{CC}} - (n-1)\varepsilon_{\mathcal{OO}}]\} \quad (1 \le n \le N). \tag{26}$$

Note that the mean-field RyR cluster model has only nine parameters: N, k^+, k^-, η, c_∞, c_*, $\varepsilon_{\mathcal{CC}}$, $\varepsilon_{\mathcal{OO}}$, and a_*.

Representative mean-field simulations

Fig. 10 *A* shows representative simulations of 25 mean-field coupled RyRs arranged according to the strength of Ca^{2+} coupling (c_*) and allosteric interactions ($\varepsilon_{\mathcal{CC}}$) used. These allosteric interactions stabilize closed channel pairs ($\varepsilon_{\mathcal{OO}} = 0$) and the average allosteric connectivity is $a_* = 0.13$, as calculated using the adjacency matrix for 25 nearest-neighbor coupled RyRs organized on a Cartesian lattice (see Fig. 1). Notice that sparks are only observed on the diagonal panels of Fig. 10 *A*, indicating that increased c_* can be compensated for by more negative $\varepsilon_{\mathcal{CC}}$. Release sites are tonically active when c_* is large and $\varepsilon_{\mathcal{CC}}$ represents weak allosteric interactions (*upper right panels*), while release sites are quiescent when c_* is small and $\varepsilon_{\mathcal{CC}}$ represents strong allosteric interactions (*lower left panels*). These mean-field results are consistent with simulations that use the full model when allosteric interactions stabilize closed channel pairs (Figs. 4 and 5, and Fig. 6 *A*). Mean-field simulations that include allosteric interactions that stabilize open channel pairs or both closed-closed and open-open channel pairs in a balanced fashion (not shown) are also consistent with the full model (Fig. 6, *B* and *C*).

The panels of Fig. 10 *B* show the birth rates ($q_{\mathrm{n,\ n+1}}$) used in each column of Fig. 10 *A* plotted as a function of the number of open channels at the release site ($n = N_{\mathcal{O}}$). Note that while the $q_{\mathrm{n,\ n+1}}$ are small when n is either small or large, the birth rates are accelerated for intermediate n, and this acceleration is enhanced as c_* increases. The panels of Fig. 10 *C* show the death rates ($q_{\mathrm{n,\ n-1}}$) used in the simulations of each row of Fig. 10 *A* plotted as a function of n. Notice that when allosteric interactions are not included in simulations (*top panel*, $\varepsilon_{\mathcal{CC}} = \varepsilon_{\mathcal{OO}} = 0$), the death rates $q_{\mathrm{n,\ n-1}}$ are a linear

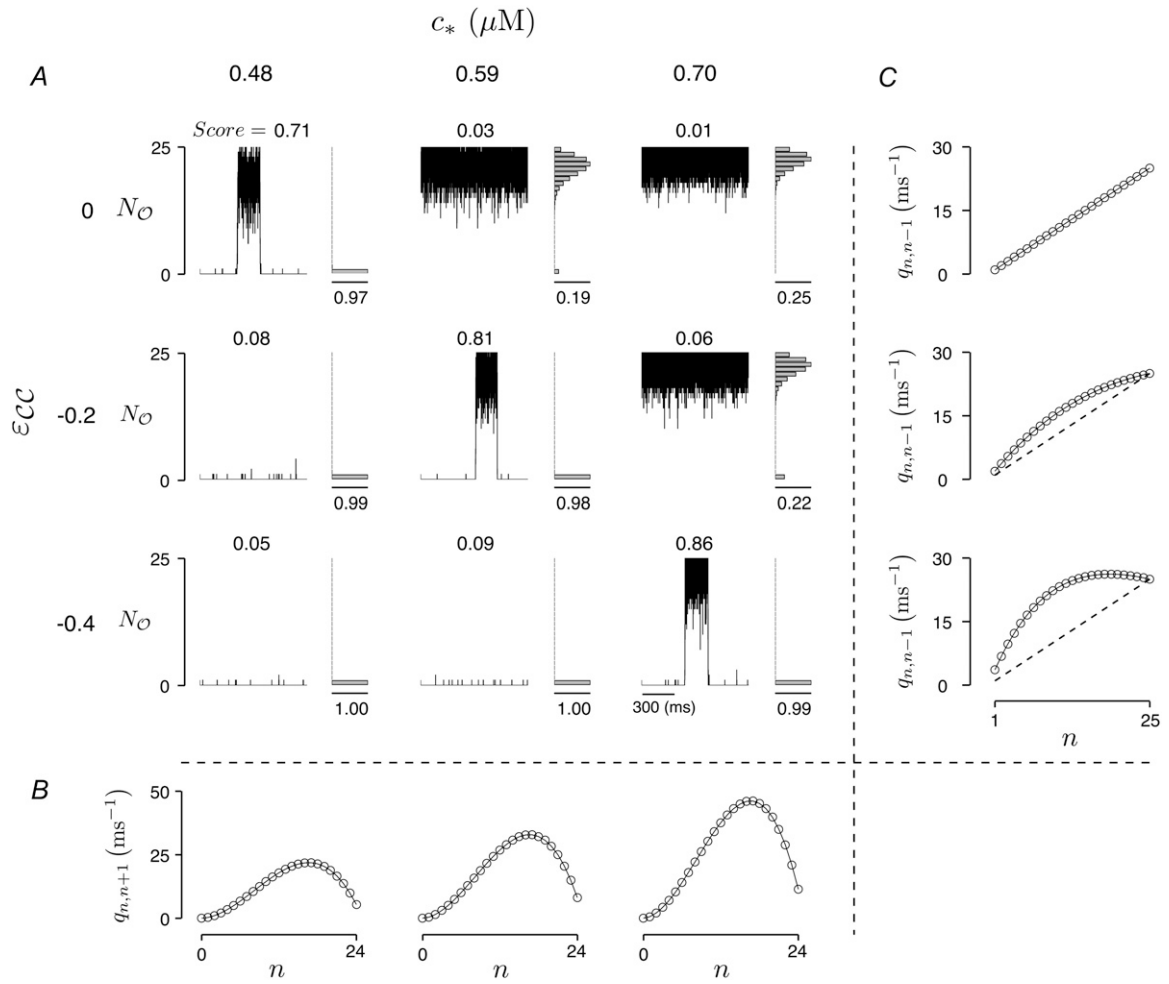

FIGURE 10 The mean-field approximation for a cluster of two-state RyRs is a birth-death process where transitions increase ($N_{\mathcal{O}} = n \rightarrow n+1$) or decrease ($N_{\mathcal{O}} = n \rightarrow n-1$) the number of open channels ($N_{\mathcal{O}}$) at the release site. (*A*) 3×3 grid showing example simulations involving 25 mean-field coupled RyRs as a function of c_* and $\varepsilon_{\mathcal{CC}}$ ($\varepsilon_{\mathcal{OO}} = 0$). The average allosteric connectivity is $a_* = 0.13$. The *Score* and steady-state probability distribution of N_{O} are also shown as calculated from Q (Appendix B). (*B*) Birth rates ($q_{\mathrm{n,\ n+1}}$) used in columns of *A* as a function of the number of open channels ($n = N_{\mathcal{O}}$). (*C*) Death rates ($q_{\mathrm{n,\ n-1}}$) used in rows of *A*. Dashed lines show the $q_{\mathrm{n,\ n-1}}$ when allosteric interactions are not included ($\varepsilon_{\mathcal{CC}} = \varepsilon_{\mathcal{OO}} = 0$). Parameters as in Table 1.

increasing function of n. However, as the magnitude of $\varepsilon_{\mathcal{CC}}$ increases, $q_{n,\,n-1}$ is accelerated for all values of $n < N$ with the most significant acceleration at intermediate n. While Fig. 10 *C* shows how the death rates change with the strength of allosteric interactions that stabilize closed channel pairs, qualitatively different changes in the death rates are observed when allosteric interactions stabilize open channel pairs, or both closed-closed and open-open channel pairs in a balanced fashion. For example, when $\varepsilon_{\mathcal{CC}} = 0$, the death rates $q_{n,\,n-1}$ decrease for all $n > 1$ as $\varepsilon_{\mathcal{OO}}$ becomes more negative. On the other hand, the birth rates $q_{n,\,n-1}$ increase for small n but decreases for large n when both $\varepsilon_{\mathcal{CC}}$ and $\varepsilon_{\mathcal{OO}}$ become more negative (results not shown).

Comparison of mean-field approximation and full model

In the previous section, we demonstrated mean-field simulations may exhibit stochastic Ca^{2+} excitability reminiscent of Ca^{2+} sparks. Similar to full model simulations, these sparks are sensitive to variations of the Ca^{2+} coupling strength (c_*) and the allosteric coupling strengths ($\varepsilon_{\mathcal{CC}}$,$\varepsilon_{\mathcal{OO}}$) used. In this section we validate the mean-field approximation by comparing the Ca^{2+} spark *Score* estimated from Monte Carlo simulations of the full model to the *Score* calculated directly from the *Q*-matrix of the corresponding mean-field model. In this comparison, the c_* and a_* of the mean-field model are calculated from the *C* and *A* of the full model, and the parameters of the single-channel models used are identical.

The symbols in Fig. 11 *A* plot the *Score* (mean ± SD of 10 trials) of Monte Carlo simulations using the full model as a function of the Ca^{2+} coupling strength (c_*) for release sites of different sizes (N) when allosteric interactions stabilize closed channel pairs ($\varepsilon_{\mathcal{CC}} = -0.2$, $\varepsilon_{\mathcal{OO}} = 0$). The dashed lines show the *Score* calculated using Q of the corresponding mean-field approximations. Both full and reduced models demonstrate that the optimal Ca^{2+} coupling strength, that is, the c_* that yields the highest *Score*, decreases as a function of N. Moreover, the range of c_* values that result in sparks (*Score* > 0.3) decreases as N increases. This inverse relationship between the optimal c_* and the release site size N, and the increase in the sensitivity of sparks to variations in c_* as N increases, are also observed when allosteric interactions stabilize open channel pairs ($\varepsilon_{\mathcal{CC}} = 0$, $\varepsilon_{\mathcal{OO}} = -0.2$) or both closed and open channel pairs in a balanced fashion ($\varepsilon_{\mathcal{CC}} = \varepsilon_{\mathcal{OO}} = -0.2$) (not shown).

Although the *Score* obtained using the full model and the mean-field approximation agree qualitatively (Fig. 11 *A*), the optimal c_* and the maximum *Score* for any given value of N show quantitative differences that becomes more evident with large N. Fig. 11 *B* shows that the *Score* (*open circles*) of simulations that use mean-field Ca^{2+} coupling ($\overline{C}$) and nearest-neighbor allosteric coupling (A) are similar to mean-field model results (*dashed line*). Similarly, the *Score* (*solid circles*) of simulations that use the full Ca^{2+} coupling matrix (C) and mean-field allosteric interactions ($\overline{A}$) show improved agreement with full model results (*open triangles*). These results suggest that the differences between the full model and the mean-field approximation are a consequence of the assumption of mean-field Ca^{2+} coupling and not the assumption of mean-field allosteric coupling.

Effect of allosteric coupling on Ca^{2+} spark statistics

The reduced state space of the mean-field approximation ($N + 1$) as opposed to the full model (2^N) greatly facilitates the calculation of spark statistics. For release site size of $N = 25$, the $2^N \times 2^N$ Q-matrices of the full model exceed the memory limitations of modern workstations; consequently, the probability distribution for $N_{\mathcal{O}}$ and the *Score* must be estimated from Monte Carlo simulation. Because the $N + 1 \times N + 1$ Q-matrices of the mean-field approximation are comparatively small, direct matrix analytic methods can be used to calculate these response measures (Appendix B) as well as spark statistics such as duration, interspark interval, and frequency (Appendix C).

In this matrix analytic approach it is convenient to reduce the number of parameters of the mean-field model via nondimensionalization. Accordingly, we express Ca^{2+} concentrations in units of the dissociation constant of Ca^{2+} binding

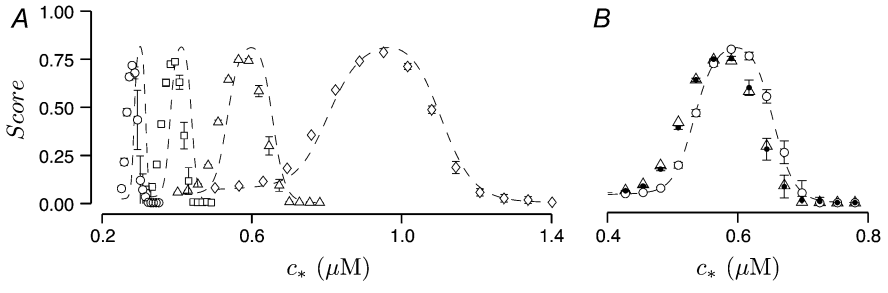

FIGURE 11 (*A*) The Ca^{2+} spark *Score* (mean ± SD of 10 trials) plotted as a function of the average Ca^{2+} coupling strength (c_*) and release site size for $N = 16$ (*diamonds*), $N = 25$ (*triangles*), $N = 36$ (*squares*), and $N = 49$ (*circles*) when allosteric coupling stabilizes closed channel pairs ($\varepsilon_{\mathcal{CC}} = -0.2$, $\varepsilon_{\mathcal{OO}} = 0$). Dashed lines show the *Score* calculated using the mean-field approximation. The average allosteric connectivity (Eq. 21) is $a_* = 0.20$ (*diamonds*), 0.13 (*triangles*), 0.095 (*squares*), and 0.071 (*circles*). Other parameters as in Table 1. (*B*) Data from simulations with $N = 25$ in *A* are expanded (*open triangles* and *dashed line*). Open circles show results from Monte Carlo simulations of the full model with nearest-neighbor allosteric coupling (A) but mean-field Ca^{2+} coupling ($\bar{C}$). Solid circles show results from simulations with mean-field allosteric coupling ($\bar{A}$) but using the full Ca^{2+} coupling matrix (C).

(K where $K^{\eta} = k^{-}/k^{+}$) and denote the nondimensional Ca^{2+} coupling strength and background $[Ca^{2+}]$ as $\hat{c}_* = c_*/K$ and $\hat{c}_\infty = c_\infty/K$, respectively. Substituting $\hat{c}_*$ and $\hat{c}_\infty$ into Eq. 23 and expressing time in units of the reciprocal of the dissociation rate constant ($1/k^{-}$), we arrive at the dimensionless generator matrix $\hat{Q} = Q/k^{-}$. After nondimensionalizing, the nine parameters of the mean-field model (N, η, $\varepsilon_{\mathcal{CC}}$, $\varepsilon_{\mathcal{OO}}$, k^{+}, k^{-}, c_∞, c_*, and a_*) are reduced to seven dimensionless parameters (N, η, $\varepsilon_{\mathcal{CC}}$, $\varepsilon_{\mathcal{OO}}$, $\hat{c}_\infty$, $\hat{c}_*$, and a_*).

Using the $\hat{Q}$ for 25 mean-field coupled RyRs, Fig. 12 shows spark duration, interspark interval, and spark frequency (*grayscale*) as a function of the strength of dimensionless Ca^{2+} coupling ($\hat{c}_*$) and allosteric interactions that stabilize closed ($\varepsilon_{\mathcal{CC}}$) and open ($\varepsilon_{\mathcal{OO}}$) channel pairs. Each panel explores a slice of this three-dimensional parameter space indicated by the shaded region of the cubes shown at the left. These correspond to allosteric interactions that stabilize closed channel pairs (Fig. 12 *A*, $\varepsilon_{\mathcal{CC}} < 0$, $\varepsilon_{\mathcal{OO}} = 0$), open channel pairs (Fig. 12 *B*, $\varepsilon_{\mathcal{CC}} = 0$, $\varepsilon_{\mathcal{OO}} < 0$), and both in a balance fashion (Fig. 12 *C*, $\varepsilon_{\mathcal{CC}} = \varepsilon_{\mathcal{OO}} < 0$). Spark statistics are only shown when sparks are present (*Score* > 0.3).

Note that similar to simulations using the full model (Figs. 6 and 7), the magnitude and range of $\hat{c}_*$ values that result in sparks increase as the strength of allosteric interactions that stabilize closed channel pairs increases (Fig. 12 *A*) and decreases as the strength of allosteric interactions that stabilize open channel pairs increases (Fig. 12 *B*). The magnitude and range of $\hat{c}_*$ values that result in sparks does not vary significantly as the magnitude of $\varepsilon_{\mathcal{CC}}$ and $\varepsilon_{\mathcal{OO}}$ increases in a balanced fashion (Fig. 12 *C*). Regardless of how stabilizing allosteric interactions are introduced, spark duration and interspark interval are increasing and decreasing functions of $\hat{c}_*$, respectively. In Fig. 12, *A–C*, spark duration increases and interspark interval decreases in such a manner that spark frequency at first increases but ultimately decreases as a function of $\hat{c}_*$.

While similar changes of spark statistics are seen as $\hat{c}_*$ increases regardless of how stabilizing allosteric interactions

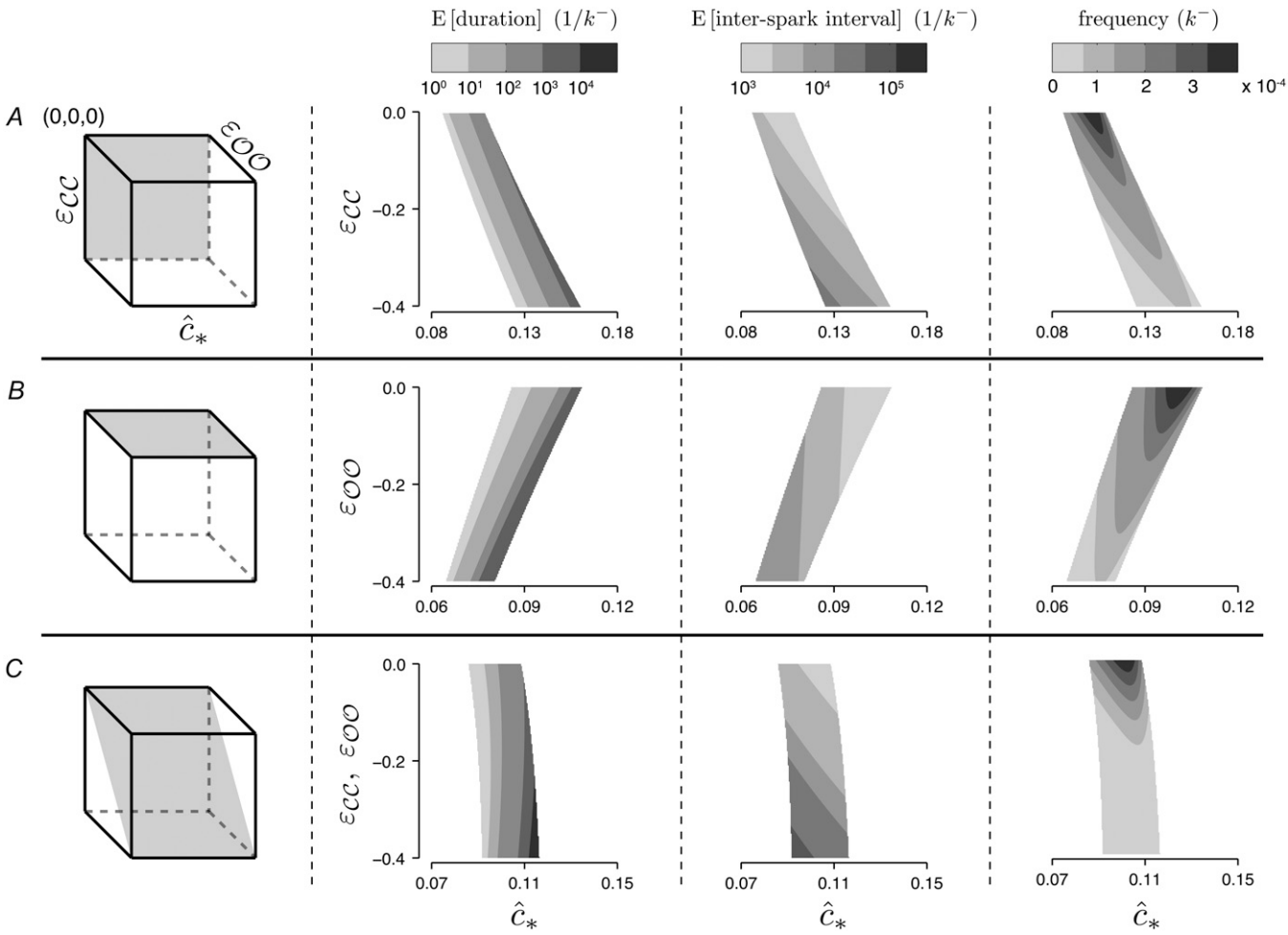

FIGURE 12 Spark duration, interspark interval, and spark frequency (in dimensionless units) of simulations involving 25 RyRs plotted as a function of the dimensionless strength of Ca^{2+} coupling ($\hat{c}_*$) and allosteric interactions when they stabilize closed channel pairs (*A*, $\varepsilon_{\mathcal{OO}} = 0$); open channel pairs (*B*, $\varepsilon_{\mathcal{CC}} = 0$); or both in a balanced fashion (*C*, $\varepsilon_{\mathcal{CC}} = \varepsilon_{\mathcal{OO}}$). Results are only shown when parameters result in robust sparks (*Score* > 0.3). The average allosteric connectivity is $a_* = 0.13$ and the dimensionless Ca^{2+} coupling strength is $\hat{c}_* = 0.01$. Other parameters as in Table 1.

are included, qualitatively different changes are observed in Fig. 12, *A–C*, as the strength of allosteric interactions increases. Fig. 12 *A* shows that increasing the strength of allosteric interactions that stabilize closed channel pairs decreases spark duration and increases interspark interval. Fig. 12 *B* shows that increasing the strength of allosteric interactions that stabilize open channel pairs increases spark duration but has little effect on interspark interval. Fig. 12 *C* shows that increasing the strength of allosteric interactions that stabilize both closed-closed and open-open channel pairs in a balanced fashion decreases interspark interval, while spark duration is largely unaffected. While in Fig. 12 *C* spark frequency is a decreasing function of the strength of allosteric interactions, in Fig. 12, *A* and *B*, spark frequency may increase, decrease, or both, depending on the coupling strength $\hat{c}_*$. Fig. 12, *A–C*, is qualitatively unchanged when the dimensionless background $[Ca^{2+}]$ ($\hat{c}_\infty$) is doubled or halved (not shown).

DISCUSSION

Although the biophysical mechanism of FK-binding protein-mediated coupling between RyRs is not well understood (13,14), several studies have presented Ca^{2+} release site models that represent physical coupling using single channel transition rates that are functions of the state of other channels at the release site (28,36,40). In this study, physical coupling between channels is implemented using a previously introduced methodology (36,53,54) where transition rates are modified by state-dependent allosteric interaction energies. In this formalism the physical coupling of N M-state channels is specified by an $M \times M$ matrix of interaction energies, a $N \times N$ adjacency matrix specifying the geometry of allosteric couplings, and a partitioning coefficient for each transition that determines how the allosteric interaction energies are divided between forward and reverse rate constants. Although this formalism does not explicitly model the binding and unbinding of RyRs or FK-binding proteins to allosteric sites on neighboring channels, Fig. 3, *B–E*, show trajectories reminiscent of experimentally observed coupled channel gating (13,14) when this methodology is used to represent stabilizing allosteric interactions. This study aims to advance our understanding of the connection between the microscopic parameters of RyR gating and the collective phenomena of Ca^{2+} sparks. The minimal formulation has facilitated extensive parameter studies investigating how the statistics of coupled gating (e.g., the Ca^{2+} spark *Score* and mean spark duration) depend on the strength of stabilizing allosteric interactions and Ca^{2+} coupling.

Allosteric coupling and Ca^{2+} spark generation and termination

A significant result of this study is the observation that synchronizing allosteric interactions always promote Ca^{2+} sparks (i.e., result in a higher *Score*) for some value of the strength of Ca^{2+} coupling (c_*), regardless of whether synchronizing allosteric interactions stabilize closed channel pairs, open channel pairs, or both (see Figs. 6 and 7). When the strength of Ca^{2+} coupling is sufficiently large to preclude termination of simulated sparks, allosteric interactions that stabilize closed channel pairs can promote spark termination. Similarly, allosteric interactions that stabilize open channel pairs facilitate spark initiation when Ca^{2+} coupling is too weak to mediate stochastic Ca^{2+} excitability. Sparks are less sensitive to variations in c_* when the strength of allosteric interactions that stabilize closed channel pairs is increased, and more sensitive to c_* when the strength of allosteric interactions that stabilize open channel pairs is increased.

Allosteric coupling washout, cardiac dysfunction, and Ca^{2+} spark statistics

A substantial body of experimental evidence demonstrates that normal cardiac function requires the association of the 12.6 kDa FK506 binding protein FKBP12.6 to the RyR channel complex (55–58). For example, pharmacological or exercise-induced PKA hyperphosphorylation of RyRs has been shown to substantially dissociate FKBP12.6 from RyRs and has been linked to increased frequency of ventricular arrhythmias and sudden cardiac death (58,59). In addition, the absence of FKBP12.6 in knockout mice has been associated with increased systolic $[Ca^{2+}]$ and cardiac hypertrophy (60).

While the connection between FKBP12.6 depletion and cardiac dysfunction is not clearly established, evidence that FK-binding proteins are responsible for coupled gating of RyRs suggests that organ-level failure may be inherited from defects in the collective gating of channels leading to irregularities in the dynamics of Ca^{2+} sparks. In striated (skeletal and cardiac) and smooth muscle, both the frequency and duration of spontaneous sparks increase upon knockout of genes encoding relevant FK-binding proteins or treatment with FK506 or rapamycin, two drugs that physically and/or functionally dissociate FK-binding proteins from RyRs (17,49,50,60–64). Conversely, overexpression of FKBP12.6 has been shown to decrease spark frequency (51). Interestingly, these experimentally observed changes in spark duration and frequency are consistent with simulated washout of allosteric interactions that stabilize closed-closed channel pairs or both closed-closed and open-open channel pairs, but inconsistent with simulations involving the washout of allosteric interactions that stabilize only open-open channel pairs (Figs. 8 and 9). While in principle these different types of allosteric coupling could leave a signature in the distribution of spark durations, this does not appear to be the case for the minimal two-state RyR model used here (Fig. 8). While these simulations aim to clarify how changes in spark statistics due to pharmacological washout of the accessory proteins mediating allosteric coupling may indicate the type

of synchronizing allosteric interactions exhibited by physically coupled RyRs, it is unclear the degree to which the results will generalize to more complicated and realistic RyR models (see below).

The mean-field approximation for allosteric interactions

The mean-field approximation formulated in this study is applicable to a cluster of RyRs coupled via both Ca^{2+} and allosteric interactions. Although this reduced model has a drastically contracted state space compared to full model simulations, the mean-field coupled RyRs exhibit Ca^{2+} sparks that are qualitatively similar to sparks of the full model (Fig. 11). However, for mean-field simulations involving a fixed number of channels and fixed allosteric coupling parameters, the Ca^{2+} coupling strength (c_*) that results in the highest *Score* is slightly elevated compared to the optimal c_* of corresponding full model simulations. This difference becomes more evident as the number of channels at release sites increases (Fig. 11), and may be a consequence of the spatial spread of activation or the clustering of open channels in full model simulations.

The mean-field reduction formulated here is analogous to the sticky cluster model of Sobie et al. (40) where the coupled gating of RyRs is represented by multiplying the $\mathcal{C} \rightarrow \mathcal{O}$ and $\mathcal{O} \rightarrow \mathcal{C}$ transition rates by cooperativity factors ($\chi_{\mathcal{O}}$ and $\chi_{\mathcal{C}}$) that depend on the number of open and closed channels in the cluster. For example, in Sobie et al. (40) the death rates are given by $q_{n,n-1} = nk^{-}\chi_{\mathcal{C}}$, where

$$\chi_{\mathcal{C}} = k_{\text{coop}}\left[1 + \frac{N_{\mathcal{C}} + 1}{N}\right], \tag{27}$$

and the scaling factor k_{coop} sets the strength of RyR coupling. By inspecting the death rates presented in this article (Eq. 26), one finds that the cooperativity factor in the mean-field model is

$$\chi_{\text{c}}' = \exp\{-a_*[(N - N_{\mathcal{O}})\varepsilon_{\mathcal{C}\mathcal{C}} - (N_{\mathcal{O}} - 1)\varepsilon_{\mathcal{O}\mathcal{O}}]\}, \tag{28}$$

which when expressed in terms of $N_{\mathcal{C}}$ is

$$\chi_{\text{c}}' = \exp\{-a_*[(N - 1)\varepsilon_{\mathcal{O}\mathcal{O}} - N_{\mathcal{C}}(\varepsilon_{\mathcal{O}\mathcal{O}} - \varepsilon_{\mathcal{C}\mathcal{C}})]\}. \tag{29}$$

Note that Eq. 27 is an increasing function of $N_{\mathcal{C}}$, consistent with Eq. 29, when $\varepsilon_{\mathcal{O}\mathcal{O}} + \varepsilon_{\mathcal{C}\mathcal{C}} < 0$, as in most of the simulations presented here. However, Eq. 29 is a nonlinear function of $N_{\mathcal{C}}$ (Eq. 27 is linear), and the scaling factor for the strength of allosteric coupling (a_*) enters Eq. 29 differently than k_{coop} in Eq. 27. Furthermore, $\chi_{\text{c}}' = 1$ when $N_{\mathcal{C}} = 0$ and $\varepsilon_{\mathcal{O}\mathcal{O}} = 0$ (and when $N_{\mathcal{O}} = 1$ and $\varepsilon_{\mathcal{C}\mathcal{C}} = 0$) regardless of the strength of allosteric coupling (not so for χ_{c} in Eq. 27). While Eq. 27 has only one free parameter (k_{coop}), we would recommend using Eq. 29 because the three parameters (a_*, $\varepsilon_{\mathcal{O}\mathcal{O}}$, $\varepsilon_{\mathcal{C}\mathcal{C}}$) are not post hoc additions to an $N + 1$ state model, but rather derived from the microscopic parameters of the 2^{N} state Ca^{2+} release site that is reduced to $N + 1$ states using the mean-field approximation. Equation 29 has the additional advantage of being able to incorporate synchronizing (or desynchronizing) allosteric interactions that stabilize (or destabilize) closed channel pairs, open channel pairs, or both. Perhaps most importantly, the comparatively small state space of mean-field coupled RyR clusters could be used to mitigate against the difficulties inherent in realistic multiscale modeling of cardiac myocyte excitation-contraction coupling (65–68).

Generalizing the mean-field approximation

Although the single-channel model used in this article includes only two states (closed and open), the mean-field approximation can be applied to clusters of channels with more complicated single-channel dynamics that include mechanisms suspected to contribute to Ca^{2+} spark dynamics in situ such as luminal regulation, Ca^{2+}-dependent inactivation, or adaptation (15,69,70). For N M-state channels there are n-choose-$k\{N + M - 1, N\}$ states in the mean-field approximation, each of which can be expressed as a vector of the form $(N_1, N_2, \cdots, N_{\text{M}})$ where N_{m} is the number of channels in state m, $1 \le m \le M$, and $\sum_{\text{m}=1}^{\text{M}} N_{\text{m}} = N$. If the current state of the release site is $(N_1, N_2, \cdots, N_{\text{M}})$ and a channel makes an $i \rightarrow j$ transition, the transition rate is $N_i k_{ij} \chi_{ij}$ and the appropriate cooperativity factor is

$$\chi_{ij} = \exp\left[-a_* \nu_{ij} \sum_{k=1}^{M} (N_k - \delta_{ki})(\varepsilon_{kj} - \varepsilon_{ki})\right], \tag{30}$$

where ν_{ij} is the previously encountered coefficient that partitions allosteric coupling between the forward and reverse transitions ($0 \le \nu_j \le 1$ and $\nu_{ji} = 1 - \nu_{ij}$), and δ_{ki} is the Krönecker delta function defined by

$$\delta_{ki} = \begin{cases} 1 & \text{if} \quad k = i \\ 0 & \text{if} \quad k \neq i \end{cases}. \tag{31}$$

Limitations of the model

A potential limitation of this study is the assumption of instantaneous coupling via the local $[Ca^{2+}]$. Theoretical studies of two-state Ca^{2+}-activated channels coupled via a time-dependent Ca^{2+} microdomain demonstrate that the time constant of Ca^{2+} domain formation and collapse can affect the dynamics of puffs and sparks (29,32). For example, slow domain formation can make the triggering of sparks less likely while slow domain collapse can prohibit the termination of Ca^{2+} release events. On the other hand, Ca^{2+} release via clusters of RyRs in ventricular myocytes occurs within dyadic clefts, spatially restricted regions of the cytosol located between the sarcolemma of T-tubules and the sarcoplasmic reticulum membrane (4,71,72). Theoretical studies indicate that the time constant of Ca^{2+} domain formation decreases as the volume of a dyad decreases and may be

<1 ms (73,74), while the decay of elevated $[Ca^{2+}]$ to background levels after termination of release may require 10s of milliseconds due to low affinity binding sites on the cytosolic face of the sarcolemma (74). Thus, in the context of Ca^{2+} release via RyR clusters in ventricular myocytes, the assumption of instantaneous coupling is more justified during the rising phase of Ca^{2+} release events than during the falling phase. Our prior work (29,30,32) suggests that this feature of the modeling formalism will increase the likelihood that all the open RyRs will close simultaneously, a mechanism referred to as stochastic attrition (15,71).

While the analysis of this article is simplified by assuming instantaneous Ca^{2+} coupling and a minimal two-state RyR, the lack of an explicit mechanism for spark termination—e.g., depletion of luminal Ca^{2+}, Ca^{2+}-dependent inactivation, or adaptation—results in sparks that terminate exclusively via stochastic attrition. Consequently, sparks of physiologically realistic durations are only observed over a finite range of Ca^{2+} coupling strengths, even when allosteric interactions are included. While allosteric interactions that stabilize closed channel pairs may potentiate spark termination via stochastic attrition when the Ca^{2+} coupling strength (c_*) is elevated (resulting in sparks that are less sensitive to c_*; see Figs. 6 *A* and 7 *A*), stabilizing allosteric interactions between closed channels do not result in robust termination of sparks at all Ca^{2+} coupling strengths. Taken as a whole, our simulations demonstrate that allosteric interactions may facilitate spark generation, and are often sufficient for spark termination in the absence of another mechanism such as depletion of luminal Ca^{2+} or Ca^{2+}-dependent inactivation. When the strength of Ca^{2+} coupling is not optimal, the strength of allosteric coupling can usually be adjusted to yield robust Ca^{2+} sparks (Fig. 12). On the other hand, for fixed allosteric coupling parameters, the range of Ca^{2+} coupling strengths leading to robust sparks was never observed to be greater than 25% of the optimal Ca^{2+} coupling strength.

While many buffers with various binding kinetics, affinities, and diffusion constants contribute to the landscape of $[Ca^{2+}]$ in vivo, the mathematical representation of the Ca^{2+} microdomain used in this article assumes a single Ca^{2+} buffer. Because the single-channel model does not include mechanisms that would promote spark termination, high buffer concentrations are required to achieve Ca^{2+} coupling strengths that allow sparks to spontaneously terminate via stochastic attrition. For example, when the RyR is modeled with dissociation constant $K_d = 5\ \mu M$ and unitary current of $i_{Ca} = 0.04$ pA, simulations that do not include allosteric interactions require $[B]_T \approx 1.2$ mM to achieve the optimal Ca^{2+} coupling strength of $c_* \approx 0.48\ \mu M$. As shown in Fig. 2 *C*, this coupling strength can be obtained using a variety of different values for $[B]_T$ or i_{Ca}; as expected, simulations using lower buffer concentrations with lower unitary current yield results that are similar to Fig. 6. When allosteric interactions stabilizing closed channel pair are included ($\varepsilon_{\mathcal{CC}} = -0.4$, *squares* of Fig. 6 *A*), the optimal coupling strength of $c_* \approx 0.71\ \mu M$ corresponds to a total buffer concentration of $[B]_T \approx 570\ \mu M$. Utilization of complex RyR gating schemes and explicit modeling of the depletion of luminal Ca^{2+} would likely decrease the total buffer concentration required for spark termination.

Perhaps the most significant limitation of this study is that the degree to which the results will generalize to more complicated and realistic RyR models is unknown. This concern is ever present when minimal single-channel models that reproduce select features of Ca^{2+}-regulation are used to study the collective gating that gives rise to Ca^{2+} sparks (28–38). Although beyond the scope of this article, it might be possible to extend inference methods commonly used in conjunction with single-channel recording (75–77) to the collective gating of mean-field coupled intracellular channels. In this way, experimentally observed statistics of sparks (e.g., the shape of the distribution of spark durations and interspark intervals) might be used to distinguish between channels that are coupled via local $[Ca^{2+}]$, allosteric interactions, or both.

For now, the generalization of our results to other single-channel models can only be addressed on a case-by-case basis. For example, in the absence of allosteric interactions, instantaneously coupled two-state RyRs do not exhibit Ca^{2+} sparks unless the cooperativity of Ca^{2+} binding is two or more ($\eta \geq 2$) (30,31). Similarly, a preliminary survey of all possible three-state single-channel models that include unimolecular Ca^{2+} binding suggests that multiple Ca^{2+}-binding transitions are required for sparks (not shown). However, when stabilizing allosteric interactions are included, cooperative Ca^{2+} binding is no longer required, that is, $\eta = 1$ can yield robust sparks (not shown).

Our validation of the mean-field approach to modeling allosteric interactions suggests that studies utilizing more realistic RyR models could be performed using the coupling factors (Eq. 30) that are derived here for the first time. Our attempts at this further analysis include simulations of mean-field coupled three-state RyRs that include a long-lived closed state (R),

$$\mathcal{C} \underset{k_a^-}{\overset{k_a^+ c^\eta}{\rightleftharpoons}} \mathcal{O} \underset{k_b^-}{\overset{k_b^+ c^\eta}{\rightleftharpoons}} \mathcal{R} \quad \text{and} \quad \mathcal{C} \underset{k_a^-}{\overset{k_a^+ c^\eta}{\rightleftharpoons}} \mathcal{O} \underset{k_a^-}{\overset{k_b^+}{\rightleftharpoons}} \mathcal{R}. \tag{32}$$

These simulations demonstrate that both Ca^{2+}-dependent and Ca^{2+}-independent inactivation often reduce the sensitivity of sparks to variations in the coupling strength (78). In preliminary studies we have found that stabilizing allosteric interactions can further extend the range of c_* values that result in robust sparks (not shown). However, it remains to be determined whether the statistics of Ca^{2+} sparks can ever be used to rule out allosteric coupling as a synchronization mechanism.

APPENDIX A: EXACT NUMERICAL SIMULATION

The Ca^{2+} release site models presented in this article are continuous-time Markov chains simulated using Gillespie's method, a numerical method with

no intrinsic time step (31,43,79). After choosing an initial release site configuration, $\boldsymbol{i} = (i_1, i_2, \ldots, i_N)$, this method requires the nonzero rates q_{ij} for the allowed transitions $\boldsymbol{i} \rightarrow \boldsymbol{j}$ to determine the subsequent release site configuration. An exponentially distributed random variable τ with mean $1/\sum_{j \neq i} q_{ij}$ is then generated giving the dwell time in the current release site configuration $\boldsymbol{i}$. The destination configuration $\boldsymbol{j}$ is selected by choosing a random variable Y uniformly distributed on a partitioned interval of length $\sum_{j \neq i} q_{ij}$ where the $\boldsymbol{i} \rightarrow \boldsymbol{j}$ transition occurs if Y falls on the partition associated with q_{ij} $(\boldsymbol{i} \neq \boldsymbol{j})$. The release site configuration as a function of time is produced by repeating these steps.

It remains to show how the q_{ij} rates are determined. When Q is sufficiently small to be held in memory, the required transition rates are the nonzero off-diagonal elements of the row corresponding to configuration $\boldsymbol{i}$. When forming Q is impractical due to memory constraints, an efficient approach is to represent the release site configuration as the $N \times M$ matrix Σ where

$$\Sigma_{nm}(t) = \begin{cases} 1 & \text{if } i_n = m, \\ 0 & \text{otherwise}, \end{cases} \tag{33}$$

and i_n is the state of channel n in release site configuration $\boldsymbol{i}$. By arranging the required transition rates in an $N \times M$ matrix $R = (r_{nm})$ where r_{nm} gives the rate at which channel n makes an $i_n \rightarrow m$ transition, these rates can be found by evaluating the matrix analytic expression,

$$\begin{aligned} R(t) = &[\Sigma \hat{K}^-] \circ \hat{\Omega}^- \\ &+ [\mathrm{diag}(c_\infty \boldsymbol{e} + C^T \Sigma \boldsymbol{u})^\eta \, \Sigma \hat{K}^+] \circ \hat{\Omega}^+, \end{aligned} \tag{34}$$

where the $\circ$ operator denotes an element $\times$ element Hadamard product. In this expression, the $M \times M$ matrices $\hat{K}^+$ and $\hat{K}^-$ are identical to K^+ and K^- (Eq. 3) but with zeros on the principal diagonals, C is the $N \times N$ Ca^{2+} coupling matrix (Eq. 8), $\boldsymbol{e}$ is a $N \times 1$ column vector of ones, and $\boldsymbol{u}$ is a $M \times 1$ column vector where entries of 0 and 1 denote closed and open states in the single-channel model. Note that the column vector $\Sigma \boldsymbol{u}$ indicates channels that are open in release site configuration $\boldsymbol{i}$, $c_\infty \boldsymbol{e} + C^T \Sigma \boldsymbol{u}$ is the $[Ca^{2+}]$ experienced by each channel, and left multiplication by the diagonal matrix $\mathrm{diag}(c_\infty \boldsymbol{e} + C^T \Sigma \boldsymbol{u})^\eta$ scales the association rate constants $(\hat{K}^+)$ by the appropriate $[Ca^{2+}]$.The matrices $\hat{\Omega}^-$ and $\hat{\Omega}^+$ that account for allosteric coupling are formed from the $N \times M$ matrix

$$\Psi = (\psi_{nm}) = A \Sigma \mathcal{E}, \tag{35}$$

where A is the $N \times N$ adjacency matrix (Eq. 12), $\mathcal{E}$ is the $M \times M$ allosteric energy matrix (Eq. 11), and ψ_{nm} is the allosteric interaction energy that channel n would experience in release site configuration Σ provided it was in state m. The elements of the $N \times M$ matrix $\Omega = (\omega_{nm})$ where $\omega_{nm} = \psi_{nm} - \psi_{n i_n}$ give the change in allosteric energy that channel n would experience if it were to make an $i_n \rightarrow m$ transition. Finally, the elements of the matrices $\hat{\Omega}^\pm = (\hat{\omega}^\pm_{nm})$ used in Eq. 34 are given by $\hat{\omega}^\pm_{nm} = \exp(-\nu^\pm \omega_{nm})$, where $\nu^\pm$ partition allosteric contributions between forward and reverse rates ($\nu^- = 1 - \nu^+$). In this article, $\nu^+ = 0$, $\hat{\Omega}^+$ is an $N \times M$ matrix of ones, and $\hat{\Omega}^- = (\hat{\omega}^-_{nm})$ where $\hat{\omega}^-_{nm} = \exp(-\omega_{nm})$.

APPENDIX B: CALCULATING THE STATIONARY PROBABILITY DISTRIBUTION

A continuous-time Markov chain model of a Ca^{2+} release site such as that considered in this article has a finite number of states and is irreducible. Consequently, the limiting probability distribution (as would be observed over an infinitely long simulation) does not depend on the initial condition. This limiting probability distribution is equal to the unique stationary distribution $\boldsymbol{\pi}$ satisfying global balance and conservation of probability (80), that is,

$$\pi Q = 0 \text{ subject to } \pi \boldsymbol{e} = 1, \tag{36}$$

where Q is the infinitesimal generator matrix, $\boldsymbol{\pi}$ is a row vector, and $\boldsymbol{e}$ is a commensurate column vector of ones.When Q is sufficiently small to be held in memory, Eq. 36 was solved by defining the stochastic matrix $W = I + Q\Delta t$, where I is a commensurate identity matrix and $\Delta t < 1/max_i |q_{ii}|$ so that $w_{ij} \geq 0$. It follows from Eq. 36 and $W\boldsymbol{e} = \boldsymbol{e}$ that $\pi W = \boldsymbol{\pi}$. Thus, $\boldsymbol{\pi}$ was found by calculating the eigenvector of W having a corresponding eigenvalue of 1.

When storage requirements for Q become excessive, $\boldsymbol{\pi}$ cannot be calculated directly. Instead, we estimate $\boldsymbol{\pi}$ from Monte Carlo simulations using

$$\pi_i \approx \frac{1}{T} \int_0^T \mathbb{1}\{\boldsymbol{S}(t) = \boldsymbol{i}\} \mathrm{d}t, \tag{37}$$

where $\mathbb{1}$ is the indictor set function and T is a sufficiently long observation period. While the T necessary for convergence of $\boldsymbol{\pi}$ may be excessive, we only require the probability distribution of the number of open channels to calculate spark statistics such as the *Score*. Because this distribution is a contraction of $\boldsymbol{\pi}$, good estimates require a substantially shorter observation window (T).

APPENDIX C: CALCULATING SPARK STATISTICS

Because the infinitesimal generator (Q) for a cluster of mean-field coupled RyRs is sufficiently small to be held in memory, the following matrix analytic method can be used to directly calculate the probability distribution of spark duration and interspark interval, as opposed to estimating these statistics from Monte Carlo simulations. Using the notation of the literature (45,81), the state space is partitioned and reorganized into aggregate classes $\mathcal{A}$ and $\mathcal{B}$ such that A is the release site configuration with no open channels ($N_\mathcal{O} = 0$) and $\mathcal{B}$ represents all configurations with $N_\mathcal{O} > 0$. As defined above, spark duration is the sojourn time in $\mathcal{B}$ assuming the sojourn begins with $N_\mathcal{O} = \kappa$ (selected to be one-fifth the release site size, i.e., $\kappa = 5$ when $N = 25$). Writing Q as

$$Q = \left(\begin{array}{c|c} Q_{\mathcal{A}\mathcal{A}} & Q_{\mathcal{A}\mathcal{B}} \\ \hline Q_{\mathcal{B}\mathcal{A}} & Q_{\mathcal{B}\mathcal{B}} \end{array} \right), \tag{38}$$

where each partition contains rates for transitions between aggregate classes, the probability density function for the spark duration (X) is given by

$$f_X(x) = -\boldsymbol{\phi} e^{x Q_{\mathcal{B}\mathcal{B}}} Q_{\mathcal{B}\mathcal{B}} \boldsymbol{e}, \tag{39}$$

where $\boldsymbol{e}$ is a $N-1 \times 1$ column vector of ones and $\boldsymbol{\phi}$ is a $1 \times N-1$ row vector containing the probability of a sojourn starting in the various states of $\mathcal{B}$. Because we define spark initiation as a $N_\mathcal{O} = \kappa - 1 \rightarrow \kappa$ transition,

$$\phi_i = \begin{cases} 1 & \text{if } i = \kappa \\ 0 & \text{otherwise} \end{cases}. \tag{40}$$

The expectation of X is found by integrating Eq. 39,

$$\mathrm{E}[X] = -\int_0^\infty x \boldsymbol{\phi} e^{x Q_{\mathcal{B}\mathcal{B}}} Q_{\mathcal{B}\mathcal{B}} \boldsymbol{e} \, \mathrm{d}x = -\boldsymbol{\phi} Q_{\mathcal{B}\mathcal{B}}^{-1} \boldsymbol{e}. \tag{41}$$

The probability density function for interspark interval can be calculated in a similar fashion and requires only that the aggregate classes $\mathcal{A}$ and $\mathcal{B}$ be redefined and Q repartitioned such that $\mathcal{B}$ represents all states with $N_\mathcal{O} \neq \kappa$ and $\mathcal{A}$ is the state with $N_\mathcal{O} = \kappa$. In this case $\boldsymbol{\phi}$ is all zeros except for the entry corresponding to $N_\mathcal{O} = 0$, which is set to unity.

This material is based upon work supported by the National Science Foundation under grants No. 0133132 and 0443843. G.D.S. gratefully acknowledges a research leave during academic year 2007–2008 supported by the College of William and Mary and a long-term visitor position at the Mathematical Biosciences Institute at Ohio State University.

REFERENCES

1. Berridge, M. J. 1993. Inositol trisphosphate and calcium signaling. *Nature*. 361:315–325.
2. Berridge, M. J. 1997. Elementary and global aspects of calcium signaling. *J. Physiol*. 499:291–306.
3. Berridge, M. J. 2006. Calcium microdomains: organization and function. *Cell Calcium*. 40:405–412.
4. Bers, D. M. 2002. Cardiac excitation-contraction coupling. *Nature*. 415:198–205.
5. Cheng, H., M. R. Lederer, W. J. Lederer, and M. B. Cannell. 1996. Calcium sparks and $[Ca^{2+}]_i$ waves in cardiac myocytes. *Am. J. Physiol*. 270:C148–C159.
6. Cheng, H., W. J. Lederer, and M. B. Cannell. 1993. Calcium sparks: elementary events underlying excitation-contraction coupling in heart muscle. *Science*. 262:740–744.
7. Franzini-Armstrong, C., F. Protasi, and V. Ramesh. 1999. Shape, size, and distribution of Ca^{2+} release units and couplons in skeletal and cardiac muscles. *Biophys. J*. 77:1528–1539.
8. Franzini-Armstrong, C., F. Protasi, and V. Ramesh. 1999. Comparative ultrastructure of Ca^{2+} release units in skeletal and cardiac muscle. *Ann. N. Y. Acad. Sci*. 853:20–30.
9. Yin, C.-C., L. M. Blayney, and F. A. Lai. 2005. Physical coupling between ryanodine receptor-calcium release channels. *J. Mol. Biol*. 349:538–546.
10. Yin, C.-C., H. Han, R. Wei, and F. A. Lai. 2005. Two-dimensional crystallization of the ryanodine receptor Ca^{2+} release channel on lipid membranes. *J. Struct. Biol*. 149:219–224.
11. Serysheva, I. I. 2005. Structural insights into excitation-contraction coupling by electron cryomicroscopy. *Biochemistry (Mosc.)*. 69:1226–1232.
12. Lai, F. A., M. Misra, L. Xu, H. A. Smith, and G. Meissner. 1989. The ryanodine receptor-Ca^{2+} release channel complex of skeletal muscle sarcoplasmic reticulum. Evidence for a cooperatively coupled, negatively charged homotetramer. *J. Biol. Chem*. 264:16776–16785.
13. Marx, S. O., K. Ondrias, and A. R. Marks. 1998. Coupled gating between individual skeletal muscle Ca^{2+} release channels (ryanodine receptors). *Science*. 281:818–821.
14. Marx, S. O., J. Gaburjakova, M. Gaburjakova, C. Henrikson, K. Ondrias, and A. R. Marks. 2001. Coupled gating between cardiac calcium release channels (ryanodine receptors). *Circ. Res*. 88:1151–1158.
15. Stern, M. D., and H. Cheng. 2004. Putting out the fire: what terminates calcium-induced calcium release in cardiac muscle? *Cell Calcium*. 35: 591–601.
16. Fill, M., and J. A. Copello. 2002. Ryanodine receptor calcium release channels. *Physiol. Rev*. 82:893–922.
17. Wang, Y.-X., Y.-M. Zheng, Q.-B. Mei, Q.-S. Wang, M. L. Collier, S. Fleischer, H.-B. Xin, and M. I. Kotlikoff. 2003. FKBP12.6 and cADPR regulation of Ca^{2+} release in smooth muscle cells. *Am. J. Physiol. Cell Physiol*. 286:C538–C546.
18. Timerman, A. P., E. Ogunbumni, E. Freund, G. Wiederrecht, A. R. Marks, and S. Fleischer. 1993. The calcium release channel of sarcoplasmic reticulum is modulated by FK-506-binding protein. Dissociation and reconstitution of FKBP-12 to the calcium release channel of skeletal muscle sarcoplasmic reticulum. *J. Biol. Chem*. 268:22992–22999.
19. Neher, E., and W. Almers. 1986. Patch pipettes used for loading small cells with fluorescent indicator dyes. *Adv. Exp. Med. Biol*. 211:1–5.
20. Sala, F., and A. Hernández-Cruz. 1990. Calcium diffusion modeling in a spherical neuron. Relevance of buffering properties. *Biophys. J*. 57: 313–324.
21. Allbritton, N. L., T. Meyer, and L. Stryer. 1992. Range of messenger action of calcium ion and inositol 1,4,5-trisphosphate. *Science*. 258: 1812–1815.
22. Wagner, J., and J. Keizer. 1994. Effects of rapid buffers on Ca^{2+} diffusion and Ca^{2+} oscillations. *Biophys. J*. 67:447–456.
23. Smith, G. D. 1996. Analytical steady-state solution to the rapid buffering approximation near an open Ca^{2+} channel. *Biophys. J*. 71: 3064–3072.
24. Gabso, M., E. Neher, and M. E. Spira. 1997. Low mobility of the Ca^{2+} buffers in axons of cultured *Aplysia* neurons. *Neuron*. 18:473–481.
25. Naraghi, M., and E. Neher. 1997. Linearized buffered Ca^{2+} diffusion in microdomains and its implications for calculation of $[Ca^{2+}]$ at the mouth of a calcium channel. *J. Neurosci*. 17:6961–6973.
26. Neher, E. 1998. Usefulness and limitations of linear approximations to the understanding of Ca^{++} signals. *Cell Calcium*. 24:345–357.
27. Smith, G. D., L. Dai, R. Miura, and A. Sherman. 2001. Asymptotic analysis of buffered calcium diffusion near a point source. *SIAM J. Appl. Math*. 61:1816–1838.
28. Hinch, R. 2004. A mathematical analysis of the generation and termination of calcium sparks. *Biophys. J*. 86:1293–1307.
29. Mazzag, B., C. J. Tignanelli, and G. D. Smith. 2005. The effect of residual Ca^{2+} on the stochastic gating of Ca^{2+}-regulated Ca^{2+} channel models. *J. Theor. Biol*. 235:121–150.
30. DeRemigio, H., and G. D. Smith. 2005. The dynamics of stochastic attrition viewed as an absorption time on a terminating Markov chain. *Cell Calcium*. 38:73–86.
31. Nguyen, V., R. Mathias, and G. D. Smith. 2005. A stochastic automata network descriptor for Markov chain models of instantaneously coupled intracellular Ca^{2+} channels. *Bull. Math. Biol*. 67:393–432.
32. Huertas, M. A., and G. D. Smith. 2007. The dynamics of luminal depletion and the stochastic gating of Ca^{2+}-activated Ca^{2+} channels and release sites. *J. Theor. Biol*. 246:332–354.
33. Rengifo, J., R. Rosales, A. González, H. Cheng, M. D. Stern, and E. Ríos. 2002. Intracellular Ca^{2+} release as irreversible Markov process. *Biophys. J*. 83:2511–2521.
34. Ríos, E., and M. D. Stern. 1997. Calcium in close quarters: microdomain feedback in excitation-contraction coupling and other cell biological phenomena. *Annu. Rev. Biophys. Biomol. Struct*. 26:47–82.
35. Shuai, J. W., and P. Jung. 2002. Optimal intracellular calcium signaling. *Phys. Rev. Lett*. 88:068102.
36. Stern, M. D., L. S. Song, H. Cheng, J. S. Sham, H. T. Yang, K. R. Boheler, and E. Ríos. 1999. Local control models of cardiac excitation-contraction coupling. A possible role for allosteric interactions between ryanodine receptors. *J. Gen. Physiol*. 113:469–489.
37. Swillens, S., P. Champeil, L. Combettes, and G. Dupont. 1998. Stochastic simulation of a single inositol 1,4,5-trisphosphate-sensitive Ca^{2+} channel reveals repetitive openings during ''blip-like'' Ca^{2+} transients. *Cell Calcium*. 23:291–302.
38. Swillens, S., G. Dupont, L. Combettes, and P. Champeil. 1999. From calcium blips to calcium puffs: theoretical analysis of the requirements for interchannel communication. *Proc. Natl. Acad. Sci. USA*. 96:13750–13755.
39. DeRemigio, H., J. Groff, and G. Smith. 2007. The spatial organization of calcium release sites and the dynamics of puffs and sparks. Biophysical Society Annual Meeting Abstracts, Program No. 1211, Baltimore, MD.
40. Sobie, E. A., K. W. Dilly, J. dos Santos Cruz, W. J. Lederer, and M. S. Jafri. 2002. Termination of cardiac Ca^{2+} sparks: an investigative mathematical model of calcium-induced calcium release. *Biophys. J*. 83:59–78.
41. Groff, J., and G. Smith. 2007. A computational investigation of the effects of allosteric coupling between ryanodine receptors on the dynamics of calcium sparks. Biophysical Society Annual Meeting Abstracts, Program No. 1209, Baltimore, MD.
42. Colquhoun, D., and A. Hawkes. 1995. A Q-matrix cookbook: how to write only one program to calculate the single-channel and macroscopic predictions for any kinetic mechanism. *In* Single-Channel Recording. B. Sakmann and E. Neher, editors. Plenum Press, New York.
43. Smith, G. 2002. Modeling the stochastic gating of ion channels. *In* Computational Cell Biology. C. Fall, E. Marland, J. Wagner, and J. Tyson, editors. Springer-Verlag, London, Heidelberg.

44. Norris, J. 1997. Markov Chains. Cambridge University Press, Cambridge, UK.

45. Ball, F. G., R. K. Milne, and G. F. Yeo. 2000. Stochastic models for systems of interacting ion channels. *IMA J. Math. Appl. Med. Biol.* 17:263–293.

46. Mejía-Alvarez, R., C. Kettlun, E. Ríos, M. Stern, and M. Fill. 1999. Unitary Ca^{2+} current through cardiac ryanodine receptor channels under quasi-physiological ionic conditions. *J. Gen. Physiol.* 113:177–186.

47. Kettlun, C., A. González, E. Ríos, and M. Fill. 2003. Unitary Ca^{2+} current through mammalian cardiac and amphibian skeletal muscle ryanodine receptor channels under near-physiological ionic conditions. *J. Gen. Physiol.* 122:407–417.

48. Guatimosim, S., K. Dilly, L. F. Santana, M. S. Jafri, E. A. Sobie, and W. J. Lederer. 2002. Local Ca^{2+} signaling and EC coupling in heart: Ca^{2+} sparks and the regulation of the $[Ca^{2+}]_i$ transient. *J. Mol. Cell. Cardiol.* 34:941–950.

49. Ji, G., M. E. Feldman, K. S. Greene, V. Sorrentino, H.-B. Xin, and M. I. Kotlikoff. 2004. RyR2 proteins contribute to the formation of Ca^{2+} sparks in smooth muscle. *J. Gen. Physiol.* 123:377–386.

50. Yoshihara, S., H. Satoh, M. Saotome, H. Katoh, H. Terada, H. Watanabe, and H. Hayashi. 2005. Modification of sarcoplasmic reticulum (SR) Ca^{2+} release by FK506 induces defective excitation-contraction coupling only when SR Ca^{2+} recycling is disturbed. *Can. J. Physiol. Pharmacol.* 83:357–366.

51. Gómez, A. M., I. Schuster, J. Fauconnier, J. Prestle, G. Hasenfuss, and S. Richard. 2004. FKBP12.6 overexpression decreases Ca^{2+} spark amplitude but enhances $[Ca^{2+}]_i$ transient in rat cardiac myocytes. *Am. J. Physiol. Heart Circ. Physiol.* 287:H1987–H1993.

52. Nicola, V. 1998. Lumping in Markov Reward Processes. Technical report, RC14719. IBM Thomas Watson Research Centre, Yorktown Heights, NY.

53. Duke, T. A., and D. Bray. 1999. Heightened sensitivity of a lattice of membrane receptors. *Proc. Natl. Acad. Sci. USA.* 96:10104–10108.

54. Duke, T. A., N. L. Novère, and D. Bray. 2001. Conformational spread in a ring of proteins: a stochastic approach to allostery. *J. Mol. Biol.* 308:541–553.

55. Lehnart, S. E., X. H. T. Wehrens, A. Kushnir, and A. R. Marks. 2004. Cardiac ryanodine receptor function and regulation in heart disease. *Ann. N. Y. Acad. Sci.* 1015:144–159.

56. Lehnart, S. E., X. H. T. Wehrens, and A. R. Marks. 2004. Calstabin deficiency, ryanodine receptors, and sudden cardiac death. *Biochem. Biophys. Res. Commun.* 322:1267–1279.

57. Wehrens, X. H. T., S. E. Lehnart, F. Huang, J. A. Vest, S. R. Reiken, P. J. Mohler, J. Sun, S. Guatimosim, L. S. Song, N. Rosemblit, J. M. D'Armiento, C. Napolitano, M. Memmi, S. G. Priori, W. J. Lederer, and A. R. Marks. 2003. FKBP12.6 deficiency and defective calcium release channel (ryanodine receptor) function linked to exercise-induced sudden cardiac death. *Cell.* 113:829–840.

58. Wehrens, X. H. T., S. E. Lehnart, S. R. Reiken, S.-X. Deng, J. A. Vest, D. Cervantes, J. Coromilas, D. W. Landry, and A. R. Marks. 2004. Protection from cardiac arrhythmia through ryanodine receptor-stabilizing protein calstabin2. *Science.* 304:292–296.

59. Marx, S. O., S. Reiken, Y. Hisamatsu, T. Jayaraman, D. Burkhoff, N. Rosemblit, and A. R. Marks. 2000. PKA phosphorylation dissociates FKBP12.6 from the calcium release channel (ryanodine receptor): defective regulation in failing hearts. *Cell.* 101:365–376.

60. Xin, H.-B., T. Senbonmatsu, D.-S. Cheng, Y.-X. Wang, J. A. Copello, G.-J. Ji, M. L. Collier, K.-Y. Deng, L. H. Jeyakumar, M. A. Magnuson, T. Inagami, M. I. Kotlikoff, and S. Fleischer. 2002. Estrogen protects FKBP12.6 null mice from cardiac hypertrophy. *Nature.* 416:334–338.

61. Xiao, R. P., H. H. Valdivia, K. Bogdanov, C. Valdivia, E. G. Lakatta, and H. Cheng. 1997. The immunophilin FK506-binding protein modulates Ca^{2+} release channel closure in rat heart. *J. Physiol.* 500:343–354.

62. McCall, E., L. Li, H. Satoh, T. R. Shannon, L. A. Blatter, and D. M. Bers. 1996. Effects of FK-506 on contraction and Ca^{2+} transients in rat cardiac myocytes. *Circ. Res.* 79:1110–1121.

63. Lukyanenko, V., T. F. Wiesner, and S. Gyorke. 1998. Termination of Ca^{2+} release during Ca^{2+} sparks in rat ventricular myocytes. *J. Physiol.* 507:667–677.

64. Acker, K. V., G. Bultynck, D. Rossi, V. Sorrentino, N. Boens, L. Missiaen, H. D. Smedt, J. B. Parys, and G. Callewaert. 2004. The 12 kDa FK506-binding protein, FKBP12, modulates the Ca^{2+}-flux properties of the type-3 ryanodine receptor. *J. Cell Sci.* 117:1129–1137.

65. Greenstein, J. L., and R. L. Winslow. 2002. An integrative model of the cardiac ventricular myocyte incorporating local control of Ca^{2+} release. *Biophys. J.* 83:2918–2945.

66. Greenstein, J. L., R. Hinch, and R. L. Winslow. 2006. Mechanisms of excitation-contraction coupling in an integrative model of the cardiac ventricular myocyte. *Biophys. J.* 90:77–91.

67. Hinch, R., J. L. Greenstein, and R. L. Winslow. 2006. Multi-scale models of local control of calcium induced calcium release. *Prog. Biophys. Mol. Biol.* 90:136–150.

68. Williams, G. S. B., M. A. Huertas, E. A. Sobie, M. S. Jafri, and G. D. Smith. 2007. A probability density approach to modeling local control of calcium-induced calcium release in cardiac myocytes. *Biophys. J.* 92:2311–2328.

69. Györke, I., and S. Györke. 1998. Regulation of the cardiac ryanodine receptor channel by luminal Ca^{2+}involves luminal Ca^{2+} sensing sites. *Biophys. J.* 75:2801–2810.

70. Györke, S. 1999. Ca^{2+} spark termination: inactivation and adaptation may be manifestations of the same mechanism. *J. Gen. Physiol.* 114:163–166.

71. Stern, M. D. 1992. Theory of excitation-contraction coupling in cardiac muscle. *Biophys. J.* 63:497–517.

72. Franzini-Armstrong, C., F. Protasi, and P. Tijskens. 2005. The assembly of calcium release units in cardiac muscle. *Ann. N. Y. Acad. Sci.* 1047:76–85.

73. Koh, X., B. Srinivasan, H. S. Ching, and A. Levchenko. 2006. A 3D Monte Carlo analysis of the role of dyadic space geometry in spark generation. *Biophys. J.* 90:1999–2014.

74. Langer, G. A., and A. Peskoff. 1996. Calcium concentration and movement in the diadic cleft space of the cardiac ventricular cell. *Biophys. J.* 70:1169–1182.

75. Ball, F. G., and M. S. Sansom. 1989. Ion-channel gating mechanisms: model identification and parameter estimation from single channel recordings. *Proc. R. Soc. Lond. B. Biol. Sci.* 236:385–416.

76. Yeo, G. F., R. K. Milne, R. O. Edeson, and B. W. Madsen. 1988. Statistical inference from single channel records: two-state Markov model with limited time resolution. *Proc. R. Soc. Lond. B. Biol. Sci.* 235:63–94.

77. Hodgson, M., and P. J. Green. 1999. Bayesian choice among Markov models of ion channels using Markov chain Monte Carlo. *Proc. Math. Phys. Eng. Sci.* 455:3425–3448.

78. Groff, J., and G. Smith. 2007. Calcium-dependent inactivation and the dynamics of calcium puffs and sparks. *J. Theor. Biol.* In press.

79. Gillespie, D. T. 1976. A general method for numerically simulating the stochastic time evolution of coupled chemical reactions. *J. Comput. Phys.* 22:403–434.

80. Stewart, W. 1994. Introduction to the Numerical Solution of Markov Chains. Princeton University Press, Princeton, NJ.

81. Ball, F., and Y. Geoffrey. 2000. Superposition of spatially interacting aggregated continuous time Markov chains. *Methodol. Comput. Appl. Probab.* 2:93–116.

82. Falke, J. J., S. K. Drake, A. L. Hazard, and O. B. Peersen. 1994. Molecular tuning of ion binding to calcium signaling proteins. *Q. Rev. Biophys.* 27:219–290.

83. Radermacher, M., V. Rao, R. Grassucci, J. Frank, A. P. Timerman, S. Fleischer, and T. Wagenknecht. 1994. Cryo-electron microscopy and three-dimensional reconstruction of the calcium release channel/ryanodine receptor from skeletal muscle. *J. Cell Biol.* 127: 411–423.